UILU-ENG 86-3611

Report No. 134

AN EXPERIMENTALLY BASED UNIFIED MODEL FOR ISOTHERMAL AND THERMO-MECHANICAL LOADING

by

Donald Slavik

Materials and Design Division
Department of Mechanical and Industrial Engineering

A Report of the

MATERIALS ENGINEERING - MECHANICAL BEHAVIOR

College of Engineering, University of Illinois at Urbana-Champaign

September 1986

ACKNOWLEDGMENT

This work was funded by the National Science Foundation, Solid and Geo-mechanics Program (Dr. K. Thirumalai, Program Director) and the Association of American Railroads, Technical Center, Chicago, Illinois (Dr. D. Stone and Mr. M. C. Fec, monitors). This support is gratefully acknowledged.

I would also like to acknowledge the support and guidance of my advisor, Professor Huseyin Sehitoglu. His time spent in discussion and review of this work is greatly appreciated.

Mr. Mark Karasek, graduate student, assisted in many of the experiments, and Mr. Richard Neu, student worker, has helped in the data analysis. I would like to thank June Kempka, Celia Daniel, and Tammy Lawhead for typing the manuscript, and Suzanne Palmer for drafting the figures.

Finally, I would like to thank my parents and fiancee, Cindy, whose patience and understanding has always been needed.

TABLE OF CONTENTS

LIST OF TABLES

Page

LIST OF FIGURES

NOMENCLATURE

A or $A(T)$	Flow rule coefficient
A_1, A_2	Area of bar 1, area of bar 2
α_{ij}	Back stress
$\bar{\alpha}$	Effective back stress or back stress
$\bar{\alpha}_{sat}$	Saturated drag stress
a, b	Back stress hardening constants
B	Drag stress hardening rate coefficient
β	Thermal coefficient of expansion
c or $c(T)$	Back stress recovery coefficient
C	Two bar model geometry term
d	Back stress recovery exponent
δ_{ij}	Kronecker delta
E	Elastic modulus
E_2	Elastic modulus of bar 2 in the two bar model
$\dot{\varepsilon}$ or $\dot{\varepsilon}_{ij}$	Total strain rate
$\dot{\varepsilon}^{e}$ or $\dot{\varepsilon}^{e}_{ij}$	Elastic strain rate
$\dot{\varepsilon}^{in}$ or $\dot{\varepsilon}^{in}_{ij}$	Inelastic strain rate
$\bar{\varepsilon}^{in}$, $\dot{\bar{\varepsilon}}^{in}$	Effective inelastic strain, effective inelastic strain rate
$\dot{\varepsilon}^{mech}$	Mechanical strain rate
$\dot{\varepsilon}^{net}$	Net strain rate
$\dot{\varepsilon}^{th}$	Thermal strain rate
ε_a	Strain amplitude
ε_{min}	Minimum strain
ε_{max}	Maximum strain

f or $f(\bar{\sigma}/K)$	Flow function
$\dot{\gamma}$	Shear strain rate
h_α	Back stress hardening function
h_k	Drag stress hardening function
$K,\dot{K}$	Drag stress, drag stress rate
K_o	Initial drag stress
K_{sat}	Saturated drag stress
ℓ_1,ℓ_2	Length of bar 1, length of bar 2
n_1,n_2	Flow rule exponents
R	Gas constant
S_1,S_2,S_3	Principal deviatoric stress components
$S_{ij},\dot{S}_{ij}$	Deviatoric stress, deviatoric stress rate
$S^c_{ij},\dot{S}^c_{ij}$	Deviatoric back stress, deviatoric back stress rate
$\sigma_{ij},\dot{\sigma}_{ij}$	Stress, stress rate
$\bar{\sigma}$	Effective stress
σ_s/μ	Shear stress normalized by the shear modulus
r_α	Back stress recovery function
r_k	Drag stress recovery function
$T,\dot{T}$	Temperature, temperature rate
$\dot{T}_{heat}$	Thermal heating rate
$\dot{T}_{cool}$	Thermal cooling rate
T_{min}	Minimum temperature
T_{max}	Maximum temperature
ν	Poisson's ratio
t	Time
Θ	Drag stress temperature dependence term

1. INTRODUCTION

1.1 Background

Engineering components are subjected to a variety of temperature and strain or stress histories in service. These histories may produce material damage that could lead to component failure. The needs of the nuclear, ground vehicle, and aerospace industries have stimulated research work in developing constitutive models to predict material stress-strain behavior under isothermal and non-isothermal loading conditions [1-3]. A general constitutive model should accurately predict observed isothermal material behavior phenomena such as cyclic transient hardening or softening to a stable state, mean stress relaxation under mean strain cycling, strain rate sensitivity, strain ratchetting under mean stress cycling, stress relaxation under strain holds, and creep behavior under stress holds [4]. The model should also be able to simulate multiaxial material response and complex temperature-strain histories.

Many constitutive models have been proposed that can predict a number of the material response characteristics listed above [3,5-20]. Time independent models based on yield surface theory have been introduced and utilized [5-10]. Accurate material response predictions have been performed with a single and multiple yield surfaces for proportional and non-proportional loading. These models can predict mean stress relaxation under mean strain cycling, ratchetting under mean stress cycling, and transient cyclic material response. They can not simulate stress relaxation under strain holds, creep straining for stress holds, or strain rate sensitive material response.

The yield surface based models were modified by adding a time dependent creep strain component to the time independent plastic strain component. This improved slow strain rate predictions where creep effects dominated [21]. Yet it could not provide accurate material simulations when a wide range of strain rates were considered. The separation of the strain rate components has also been found to be unjustified on a microstructural basis. Since creep and plasticity both result from dislocation generation, motion, and annihilation, the inelastic strain components should interact. This interaction has been found experimentally [1,4,19], making a separate treatment unjustified.

A more accurate time dependent constitutive model is needed for high temperature material design. Unified theories have been proposed that did not separate plastic and creep strain components, but treated them in a unified manner as inelastic strain [3,11-20]. The unified theories were based on a state representation that included hardening and recovery functions consistent with the Bailey-Orowan theory [22,23]. These theories have the potential to predict material response for creep and cyclic plasticity subjected to isothermal and thermo-mechanical loading once the constitutive equations and material constants are established.

In early studies, a single state variable unified model had been implemented for monotonic rate-dependent material response [11,13]. The single state variable model utilized an isotropic drag stress that evolved throughout the deformation history. The model had also been modified to account for cyclic deformation with two isotropic state

variables [12] which produced accurate cyclic predictions, but was susceptible to instabilities, particularly at low temperatures [21].

Two state variable unified models were also introduced to account for combined isotropic and kinematic hardening [3,14-20]. These models are capable of predicting transient material response, mean stress relaxation, strain hold stress relaxation, cyclic plasticity, and stress hold creep. Thermo-mechanical simulations have also been performed [3,18-21], but only for limited temperature-strain histories in many cases.

A wide range of temperature-strain histories should be (but rarely are) considered to identify model shortcomings and limitations. Many unified models may be inaccurate for low temperature simulations where many engineering materials exhibit rate insensitive material behavior [3,14,18]. Low temperature rate insensitive material behavior may occur if a different mechanism is activated that is not present in the high temperature experiments that are usually used to determine material constants. Different deformation mechanisms have been identified in deformation mechanisms maps [24], but are rarely considered in constitutive model development. A constitutive model is needed that can account for relative rate insensitive material behavior obtained at low temperatures, as well as highly rate sensitive material behavior observed at high temperatures.

An experimentally based unified model will be presented that accounts for different deformation mechanisms. The constitutive functions will not be chosen a priori, but will be derived directly from experiments. The model capabilities will be presented to produce

relative rate insensitive and rate sensitive material behavior obtained at different temperatures. The model will then be checked with critical thermo-mechanical experiments that are independent of those that provide the material constants.

1.2 Purpose and Scope

In this study:

(1) An experimentally based unified model will be presented for isothermal and thermo-mechanical loading.

(2) A consistent systematic method will be presented for determining the model constants.

(2) The model will be capable of accounting for different deformation mechanisms that may occur when a wide range of strain rates and temperatures are considered.

(3) The model will be checked with critical independent thermo-mechanical experiments with different temperature ranges and temperature-strain histories.

2. EXPERIMENTAL PROCEDURE

The material examined was a 1070 steel (Class U) typically used in railroad wheels. Isothermal and thermo-mechanical computer controlled tests have been performed on this material with smooth specimens. For the isothermal tests, a three zone resistance furnace was used with a 20 kip MTS load frame. Stress, strain, and temperature were continuously recorded and stored. For more details on the experimental techniques, refer to Ref. [25-27].

For the thermo-mechanical tests, the two bar model was utilized. Two bars in parallel are shown in Fig. 1a. In this case, bar 2 is assumed to remain isothermal and elastic while bar 1 is subjected to a temperature history. Two bars in series are shown in Fig. 1b. In this case, bar 2 is assumed to remain elastic while both bars undergo the same temperature history. The governing axial strain rate equation for bar 1 can then be derived from equilibrium and compatibility requirements as

$$\dot{\varepsilon}^{mech} + \dot{\varepsilon}^{th} = \dot{\varepsilon}^{net} = \frac{\dot{\sigma}}{E_2 C} \qquad \text{(parallel bar model, Fig. 1a)}$$

$$\dot{\varepsilon}^{mech} + \dot{\varepsilon}^{th} = \dot{\varepsilon}^{net} = \frac{\dot{\sigma}}{E_2 C} - \frac{\ell_2}{\ell_1}\dot{\varepsilon}^{th} \qquad \text{(series bar model, Fig. 1b)} \tag{1}$$

where $\dot{\varepsilon}^{mech}$ is the mechanical strain rate which is the sum of the elastic strain rate and the inelastic strain rate, $\dot{\varepsilon}^{th}$ is the thermal strain rate, $\dot{\varepsilon}^{net}$ is the net or total strain rate, $\dot{\sigma}$ is the stress rate on bar 1, E_2 is the elastic modulus of bar 2, A_1, A_2, ℓ_1, and ℓ_2 are respective bar areas and lengths, and $C = A_2\ell_1/A_1\ell_2$ and ℓ_2/ℓ_1 are geom-

etry terms that provide different constraint conditions. Bar 1 in the two bar model is heated with a 2.5 kW induction heater and is allowed to cool in the laboratory air. The net strain was measured throughout the tests with a high temperature 25.4 mm axial extensometer with quartz rods. The test system schematic is shown in Fig. 2. A detailed discussion of the two bar model can be found in Ref. 25,26.

3. TIME-DEPENDENT MATERIAL BEHAVIOR

3.1 The Unified Theory and the State Representation

The concept of a material state was presented in the development of the unified theory [3,11-20]. Two state variables were found to be sufficient in representing combined isotropic and kinematic hardening. The two state variables possess the physical interpretation in deviatoric stress space shown in Fig. 3. The drag stress state variable, K, is related to the stress surface size. The deviatoric back stress state variable, S^c_{ij}, represents the stress surface center in deviatoric stress space. The effective stress $\bar{\sigma}$, is a measure of the distance between the current stress S_{ij}, and the current deviatoric back stress S^c_{ij}.

In the unified theories, inelastic flow may occur inside the stress surface, though it will be small. The stress state can also move outside the stress surface, where inelastic flow occurs readily. The internal state will evolve throughout the deformation history in a recovery-hardening formal as,

$$\dot{S}^c_{ij} = \frac{2}{3} h_\alpha \dot{\varepsilon}^{in}_{ij} - r_\alpha S^c_{ij} \tag{2}$$

$$\dot{K} = h_k - r_k + \theta \dot{T} \tag{3}$$

where $\dot{S}^c_{ij}$ is the deviatoric back stress rate, S^c_{ij} is the deviatoric back stress, $\dot{\varepsilon}^{in}_{ij}$ is the inelastic strain rate, $\dot{K}$ is the drag stress rate, $\dot{T}$ is the temperature rate, θ is the drag stress temperature dependence term, h_α and h_k are the hardening functions, and r_α and r_k are the

recovery functions. In general the hardening and recovery functions are dependent on the temperature, the drag stress, the effective back stress, $\bar{\alpha}$, and the effective stress, $\bar{\sigma}$. The effective quantities are

$$\bar{\alpha} = \sqrt{\frac{3}{2} S^c_{ij} S^c_{ij}} \tag{4}$$

$$\bar{\sigma} = \sqrt{\frac{3}{2} (S_{ij} - S^c_{ij})(S_{ij} - S^c_{ij})} \tag{5}$$

where the deviatoric stress is related to the stress, σ_{ij}, as

$$S_{ij} = \sigma_{ij} - \frac{1}{3} \delta_{ij} \sigma_{kk} \tag{6}$$

where δ_{ij} is the Kronecker delta, and the deviatoric back stress is related to the back stress, α_{ij}, as

$$S^c_{ij} = \alpha_{ij} - \frac{1}{3} \delta_{ij} \alpha_{kk} \tag{7}$$

The inelastic strain rate components are determined with the flow rule that is a function of the internal state. The flow rule will be taken as a function of the effective stress normalized by the drag stress, or

$$\dot{\varepsilon}^{in}_{ij} = \frac{3}{2} f[\frac{\bar{\sigma}}{K}] \frac{S_{ij} - S^c_{ij}}{\bar{\sigma}} \tag{8}$$

where $f(\bar{\sigma}/K)$ is the flow function and the last term in equation 8 produces the individual inelastic strain rate components for multiaxial loading.

The functions f, r_α, h_α, h_k, r_k, and θ need to be determined from experiments. A systematic method will be presented for determining each functional form and the model constants.

3.2 Strain Rate Sensitivity and Deformation Mechanisms

The unified constitutive model should be capable of producing complex time dependent material response for a wide range of temperatures and strain rates. Figure 4(a) shows constant strain rate material response schematically. The strain rate is increasing by a factor of 10. For the slow strain rate regime ($\dot{\varepsilon} < 10^2 c$), the material exhibits a high degree of strain rate sensitivity. In this slow strain rate regime, decreasing the strain rate by a factor of 10 will significantly decrease the measured stress response. For the fast strain rate regime ($\dot{\varepsilon} > 10^3 c$), the material exhibits a low degree of strain rate sensitivity. Increasing the strain rate by a factor of 10 in this regime does not significantly increase the measure stress response. The different degrees of strain rate sensitivity can also be observed by considering different temperatures. In Fig. 4(b) the material response at two strain rates ($\dot{\varepsilon} = c$ and $10c$) is shown at a low temperature ($T = T_{low}$) and at a high temperature ($T = T_{high}$). At the low temperature, the material is rate insensitive, while the material is rate sensitive at the higher temperature for the same strain rates.

The different strain rate sensitivity regimes at different strain rates and temperatures are due to different microstructurally activated deformation mechanisms that have been identified by Frost and Ashby [24] and should be included in constitutive models. A deformation mechanism

map for 304 stainless steel is shown in Fig. 5 as an example. (A similar map could also be constructed for 1070 steel). The shear strain rate, $\dot{\gamma}$, is plotted versus the shear stress normalized by the shear modulus, σ_s/μ. Isotherms are shown by the thin solid lines through the diffusional flow, power law creep, and plasticity deformation mechanism regimes.

The plasticity mechanism dominates for combinations of high stresses and fast strain rates where the material exhibits rate insensitive flow for constant strain rate experiments. Here, the inelastic strain rate is exponentially related to the stress which corresponds to the steep slopes of the isotherms on the deformation map.

The power law creep mechanism dominates for combinations of intermediate stresses and temperatures. The material exhibits a high degree of strain rate sensitivity for constant strain rate cases. For the power law creep mechanism, the strain rate is proportional to the stress raised to a constant exponent.

When diffusional flow is the operative mechanism, the inelastic strain rate is proportional to the stress (stress exponent is unity). Diffusional flow dominates for combinations of low strain rates, high temperatures, and low stresses.

The different deformation mechanisms influence time dependent material response significantly, and will be incorporated into the proposed constitutive model.

4. THE EXPERIMENTALLY BASED UNIFIED CONSTITUTIVE MODEL

4.1 The Flow Rule

The flow rule (Eq. 8) is used to calculate the inelastic strain rate as a function of the material internal state. The flow rule should account for different deformation mechanisms that lead to different strain rate sensitivity regimes [28]. By considering a wide range of testing conditions and three simplifying assumptions regarding the material internal state, it is possible to determine the functional form of the flow rule directly from experiments.

1) First, assume that a set of specimens exist that are identical prior to testing.

This group of specimens that are identical should initially possess the same internal state.

2) Secondly, assume that the internal state is known, or can be measured either directly or indirectly from experiments.

The initial back stress can be measured from the material anisotropy. If the material is isotropic in the virgin state, the back stress is initially identically zero. The initial drag stress, K_o, is determined from the material yield stress which can also be measured.

3) Finally, assume that the material state does not evolve to some new internal state until appreciable inelastic flow occurs.

Nearly elastic flow will not change the material internal state as long as very high temperatures are not considered where material annealing (recovery) is significant.

With these three assumptions and a set of isothermal constant strain rate, constant stress rate, and/or stress hold creep experiments, the flow rule can be determined directly from experiments. A small inelastic offset can be used to measure the stress and the inelastic strain rate for these tests. If the offset is small, the material internal state will not have evolved appreciably from the initial conditions (assumptions 3) which are known (assumption 2). Inelastic strain rate versus yield stress measurements for 1070 steel is shown in Fig. 6. For high temperatures ($T \geq 600^{o}C$ for 1070 steel), a strong strain rate dependence exists on the yield stress. This is characteristic of the power law creep mechanism. For lower temperatures, the material exhibits relative strain rate insensitivity. This is characteristic of the plasticity deformation mechanism.

The horizontal axis in Fig. 6 can be normalized for different temperatures by taking K_o as the yield stress at the plasticity-power law creep mechanism intersection. At 400°C, both mechanisms have been observed experimentally for the strain rate considered, which allows for the drag stress to be determined directly. For other temperatures where extensive strain rate measurements are not available, it is possible to get an approximate measure for the drag stress. Taking K_o/E = constant, where E is the elastic modulus, K_o is determined as a function of

temperature. The elastic modulus temperature dependence is shown in Fig. 7. With the 400°C measurements, $K_o/E = 1.3 \times 10^{-3}$ for 1070 steel.

With this procedure, plasticity is the governing deformation mechanism for stress states outside the stress surface, and power law creep is the governing deformation mechanism for stress states on and inside the stress surface. Diffusional flow has not been encountered since low stress and low strain rate experiments have not been performed.

The flow rule that fits the experimental measurements is

$$\dot{\varepsilon}^{in}_{ij} = \frac{3}{2} A\left(\frac{\bar{\sigma}}{K}\right)^{n_1} \frac{(S_{ij} - S^c_{ij})}{\bar{\sigma}} \quad \text{for } \frac{\bar{\sigma}}{K} \leq 1 \tag{9}$$

and

$$\dot{\varepsilon}^{in}_{ij} = \frac{3}{2} A \exp\left[\left(\frac{\bar{\sigma}}{K}\right)^{n_2} - 1\right] \frac{(S_{ij} - S^c_{ij})}{\bar{\sigma}} \quad \text{for } \frac{\bar{\sigma}}{K} > 1 \tag{10}$$

where A, n_1, and n_2 are material constants. The flow rule for 20°C to 700°C is shown in Fig. 8 for 1070 steel. The effective inelastic strain, $\dot{\bar{\varepsilon}}^{in}$, in Fig. 8 is

$$\dot{\bar{\varepsilon}}^{in} = \sqrt{\frac{2}{3} \dot{\varepsilon}^{in}_{ij} \dot{\varepsilon}^{in}_{ij}} \tag{11}$$

The high slope in the plasticity mechanism regime corresponds to rate insensitive material behavior as observed on the deformation mechanism map. The lower slope (n_1) of the power law creep deformation mechanism corresponds to rate sensitive material behavior. The temperature de-

pendence of $A = A(T)$ is shown in Fig. 9 where $A = A' \exp[-\Delta H/R\ (T + 273)]$.

4.2 The Back Stress

The back stress state variable is important for stress hardening materials. As suggested by Onat [16,29], it is possible to get a measure of the internal state for uniaxial loading with a rapid unloading-reloading cycle shown in Fig. 10. The material is taken to start at zero stress and strain in some initial state. The material state will then evolve throughout the deformation history O-A. At point A it is possible to run a very fast cycle B-B' to get a measure of the material state at A. The mean stress of cycle B-B' is a measure of the material anisotropy and is equal to the back stress. The elastic range will correspond to twice the drag stress 2K. If the cycle B-B' is very fast and has a small inelastic strain range, it will not change the internal state significantly, but will provide a measure of the internal state at A, and allow the test to be continued (shown by the dashed line). However, at high temperatures it is very difficult to run the cycle B-B' fast enough such that recovery and time dependent affects are insignificant. This requires approximate state measurement techniques to determine the evolution equations for high temperature rate sensitive behavior.

The back stress can be measured approximately from the monotonic reversal as the current stress subtracted from the material yield stress shown schematically in Fig. 11. For very low temperatures ($T = 20°C$ for 1070 steel), the recovery term will be negligibly small (the stress will

not saturate except at very large strains), and the stress hardening can be measured to determine h_α from the $\bar{\alpha} - \bar{\varepsilon}^{in}$ plot (Fig. 12). For reverse plasticity ($\alpha_{ij}\,\dot{\varepsilon}^{in}_{ij} < 0$), the back stress will decrease in magnitude rapidly. The evolution of α_{ij} for reverse plasticity must be established by considering the cyclic response and noting that h_α is continuous around $\alpha_{ij} = 0$.

The recovery function r_α is determined with steady state material response where $\dot{\bar{\varepsilon}}^{in}$ = constant and $\dot{\bar{\sigma}} = 0$, so $\dot{\alpha}_{ij} = \dot{K} = 0$. Steady state stress hold creep response or saturated constant strain rate monotonic response can be used (Fig. 11). Equation (2) can be rearranged to determine r_α for different values of α_{ij} and temperature. For $r_\alpha = c(|\bar{\alpha}|)^d$, the exponent d is determined as shown in Fig. 13a. The coefficient $c = c(T)$, is determined as shown in Fig. 13b, where $c = c'\exp[-G/R(T+273)]$.

4.3 The Drag Stress

The initial drag stress K_0 can been established by examining the inelastic strain rate-stress response. The evolution of the drag stress can be determined by examining the cyclic material response. A small inelastic offset can be used to measure the cyclic unloading-reloading elastic range which is related to 2K. The drag stress hardening function considered that can produce cyclic hardening or softening to the stable state is

$$h_k = B\,[K_{sat} - K]\dot{\bar{\varepsilon}}^{in} \qquad (12)$$

where K_{sat} and B are material constants, and $\dot{\bar{\varepsilon}}^{in}$ is the effective inelastic strain rate. For $K_{sat} > K$, the material will cyclically harden, or $\dot{K} > 0$. For $K_{sat} < K$, the material will soften, or $\dot{K} < 0$. For $K_{sat} = K$, the material is cyclically stable, or $\dot{K} = 0$. The constant K_{sat} was determined from the saturated response in cyclic tests ($\varepsilon_a = 1.0\%$). The constants K_o and K_{sat} versus temperature are shown in Fig. 14. The material cyclically hardens significantly at intermediate temperatures (100°C < T < 400°C), and hardens a small degree at low temperatures (T < 100°C) and at high temperatures (T > 500°C). The hardening or softening rate to the saturated response is controlled by the constant B. By rearranging Eq. (12) it is possible to determine B directly from experiments (Fig. 15). The hardening rate is taken to be temperature insensitive.

The recovery term r_k is important when material annealing becomes significant. To determine r_k, two specimens can be work hardened with a cyclic history. After a set amount of work hardening has been completed, both specimens can be subjected to an incremental strain step down history shown schematically in Fig. 16(a). The step down will reduce the back stress to approximately zero, while the material retains its work hardened state ($\alpha \rightarrow 0$, $K \geq K_o$). The subsequent work hardened stress-strain response after the step-down for specimen 1 is shown schematically in Fig. 16(b) by the dashed line. The second specimen is heated at zero stress to a temperature that will produce annealing. Specimen 2 can then be cooled and the subsequent stress strain material response (with the drag stress recovery) is shown in Fig. 16b by the solid line. The changes in drag stress for each test can be measured

and related to the drag stress recovery term r_k. For the temperature range of interest for 1070 steel ($T < 700°C$), annealing effects are small and the recovery term r_k will be neglected.

The thermally activated term θ accounts for the temperature dependence of the drag stress and any thermally activated mechanisms that may not be present in isothermal loading. In this study the temperature dependence of the drag stress is accounted for in a simple way as $\theta = \partial K_o / \partial T$.

5. MODEL PREDICTIONS AND EXPERIMENTAL RESULTS

5.1 Isothermal Loading

The constitutive model functions are given in Table 1. The material constants for 1070 steel are given in Table 2. Model capabilities to produce complex rate dependent material behavior at different temperatures are shown in Figs. 17 through 19. At 20°C (Fig. 17), the material response is relatively rate insensitive for $\dot{\varepsilon} = 10^{-10}$ sec^{-1} to $\dot{\varepsilon} = 10^{0}$ sec^{-1}. At 400°C (Fig. 18), the material response is rate sensitive for strain rates slower than 10^{-6} sec^{-1} where power law creep is the dominant deformation mechanism. For strain rates faster than 10^{-4} sec^{-1}, the material response becomes rate insensitive as the plasticity mechanism dominates. At 600°C (Fig. 19), the material exhibits a strong degree of rate sensitivity over the entire regime of strain rates considered.

Cyclic model predictions are compared to experiments for 20°C to 700°C in Figs. 20 through 28. Cycles are plotted out logarithmically (1,2,4,8,16,32,...) to capture the initial and the stable cyclic stress strain response. Cycle numbers are given next to the hysteresis loops at the maximum stress. The temperature and strain rate is shown on each figure.

A mean strain simulation has been performed to check the model capabilities to produce mean stress relaxation. In Fig. 29, a 20°C mean stress relaxation prediction and the corresponding experimental material response is shown. The predicted mean stress approached zero faster than expected, but the overall material response characteristics is captured.

Stress hold relaxation predictions are shown in Figs. 30 and 31 for 400°C and 600°C, respectively. The predicted stress strain response and also the stress-time response is given. The stress relaxed during the strain hold for both cases considered. No experimental results were available for comparison.

The back stress-strain evolution for cyclic tests ($\dot{\varepsilon}$ = 0.002 sec^{-1}) at 20°C, 300°C, and 600°C, are shown in Fig. 32. For 20°C and 400°C, the recovery term (r_α) is small, and during elastic unloading the back stress remains approximately constant (Figs. 32a and 32b). During reverse plastic loading the back stress decreases in magnitude rapidly to zero before increasing in magnitude gradually, capturing the stress hardening behavior. At 600°C, the recovery term is significant, and the back stress decreases during elastic unloading. The back stress then decreases to zero during reverse loading before saturating to a constant value (Fig. 32c).

The drag stress evolution for the same cyclic tests is shown in Fig. 33. The initial drag stress ($K = K_o$ at $t = 0$) decreases with increasing temperature. At 20°C and 600°C the drag stress remains nearly constant which corresponds to the stable fully reversed cyclic response observed. At 300°C, the drag stress increases significantly. This increase corresponds to a large degree of cyclic hardening. The model is capable of producing different transient response characteristics at different temperatures.

5.2 Thermo-Mechanical Loading

The constitutive model has also been checked with independent thermo-mechanical loading experiments. Various temperature ranges and different temperature-net strain histories have been performed utilizing the two bar structure (Fig. 1). The specimen simulating bar 1 is heated, and is forced into compression due to the constraint of bar 2. If bar 1 is heated far enough, it may yield in compression. The stresses in compression may then start to drop off if the material strength decreases with temperature. As the bar is cooled, the stress direction reverses and tensile yielding may occur.

Experimental and predicted thermo-mechanical material response for bar 1 in the two bar model is shown in Figs. 34-37 for different constraint conditions. The parallel bar model (Fig. 1a) is used for total constraint material response shown in Fig. 34 ($C \to \infty$, $\dot{\varepsilon}^{net} = 0$) and for partial constraint material response shown in Fig. 35 ($C = 1$, $\dot{\varepsilon}^{net} = -\dot{\sigma}/E_2$). The series bar model (Fig. 1b) is used to identify the over constraint condition shown in Figs. 36-37 ($C \to \infty$ and $\ell_2/\ell_1 = 1$, $\dot{\varepsilon}^{net} = -\dot{\varepsilon}^{th}$). The mechanical, thermal, and net strain versus stress response is given in Figs. 34-37.

The temperature rates for each thermo-mechanical experiment is given in Table 3. The temperature rates can be used to calculate the mechanical strain rate of the thermo-mechanical histories. In general, the heating rate was faster than the cooling rate, but the average mechanical strain rate is approximately 0.00015 sec^{-1} for the partial and total constraint histories, and the rate is on the order of 0.0002 sec^{-1} for the over constraint histories.

Total constraint ($\dot{\varepsilon}^{net} = 0$, $\dot{\varepsilon}^{mech} = -\dot{\varepsilon}^{th}$) has also been examined in depth for different temperature ranges. Figures 38 through 41 show various mechanical strain-stress plots for different total constraint conditions. Predictions compare favorably with the experiments.

6. DISCUSSION

An experimentally based unified creep-plasticity constitutive model has been developed for isothermal and thermo-mechanical loading. The functional forms were not chosen a priori, but established directly from the experiments. A systematic non-iterative method is presented for determining the material constants from standard isothermal creep and constant strain rate tests. Deformation mechanisms were incorporated into the constitutive model to produce complex time dependent material response for temperatures ranging from 20°C to 700°C. At 20°C, the material model simulated material behavior that was relatively rate insensitive (Fig. 17). At higher temperatures ($T > 400°C$ for 1070 steel), the model simulated material behavior that was highly rate sensitive (Fig. 19). The model was also able to produce different rate sensitivity regimes at the intermediate temperatures (Fig. 18).

Thermo-mechanical predictions independent of the thermo-mechanical experiments provide a critical check on the material model. For the thermo-mechanical experiments, different deformation mechanisms are activated throughout the temperature-strain history. At the low temperature end, the material may be rate insensitive where plasticity is the governing deformation mechanism. At the high temperature end, the material may be highly rate sensitive if power law creep is the governing deformation mechanism. Since the model accounts for both mechanisms and the complex time dependent response that result from them, the predictions match the experimental response for the thermo-mechanical cases considered.

It would also be instructive to check the model with non-proportional loading histories. Additional hardening observed in non-proportional loading [10,11] may be readily incorporated into the constitutive model.

7. CONCLUSIONS

1) Deformation mechanisms influence material behavior and should be incorporated into unified creep-plasticity constitutive models to provide accurate temperature and strain rate effects.

2) Material behavior over a wide range of temperatures and strain rates should be studied in constitutive model development and evaluation.

3) Loading histories independent of the experiments required to derive the material constants should be considered in constitutive model development. In this study critical independent thermo-mechanical histories were considered for constitutive model evaluation.

4) The choice of hardening and recovery functions and the flow rule a priori places an undesirable and misleading constraint on the constitutive equations. The functions may be readily established from experiments as illustrated in this study.

Table 1 Constitutive Functions for 1070 Steel

Strain Components

$$\dot{\varepsilon}^{th} = \beta \dot{T}$$

$$f(\bar{\sigma}/K) = \begin{cases} A(\bar{\sigma}/K)^{n_1} & \text{for } \bar{\sigma}/K \leq 1 \\ A \exp[(\bar{\sigma}/K)^{n_2} - 1] & \text{for } \bar{\sigma}/K > 1 \end{cases}$$

$$\dot{\varepsilon}^{e}_{ij} = [(1-\nu)\,\dot{\sigma}_{ij} - \nu \dot{\sigma}_{kk}\delta_{ij}]/E - [(1-\nu)\sigma_{ij} - \nu\sigma_{kk}\delta_{ij}]\,\frac{\partial E}{\partial T}\,\dot{T}/E^2$$

Back Stress Evolution

$$h_\alpha = \begin{cases} a - b\bar{\alpha} & S^c_{ij}\,\dot{\varepsilon}^{in}_{ij} \geq 0 \\ a & S^c_{ij}\,\dot{\varepsilon}^{in}_{ij} < 0 \end{cases}$$

$$r_\alpha = c(\bar{\alpha}/\alpha^*)^d$$

Drag Stress Evolution

$$h_k = B(K_{sat} - K)\,\dot{\bar{\varepsilon}}^{in}$$

$$r_k = 0$$

Table 1 (continued)

where

$$\bar{\sigma} = \sqrt{\frac{3}{2}(S_{ij} - S^c_{ij})(S_{ij} - S^c_{ij})}$$

$$\bar{\alpha} = \sqrt{\frac{3}{2} S^c_{ij} S^c_{ij}}$$

$$\dot{\bar{\varepsilon}}in = \sqrt{\frac{2}{3} \dot{\varepsilon}in_{ij} \dot{\varepsilon}in_{ij}}$$

$$A = A'\exp[-\Delta H/R(T + 273)]$$

$$c = c'\exp[-G/R(T + 273)]$$

$$E = e_1 - e_2 T$$

$$K_o = h_1 - h_2 T$$

$$\Theta = -h_2$$

$$K_{sat} = h_3 + h_4 T + h_5 T^2$$

Table 2 Material Constants for 1070 Steel

β = $1.7 \times 10^{-5}/°C$

A' = 4.0×10^{9} sec^{-1}

ΔH = 210.6 KJ/mole

n_1 = 5.4

n_2 = 8.3

ν = 0.3

a = 48,000 MPa

b = 100

α^* = 100 MPa

c' = 6.0×10^{14} sec^{-1}

G = 249.0 KJ/mole

d = 3.3

B = 5.0

For $T \leq 440°C$

e_1 = 202250 MPa, e_2 = 31.0 MPa/°C

h_1 = 262.7 MPa, h_2 = 0.04 MPa/°C

For $T > 440°C$

e_1 = 309990 MPa, e_2 = 275.7 MPa/°C

h_1 = 403.0 MPa, h_2 = 0.36 MPa/°C

For $T \leq 304°C$

h_3 = 256.0 MPa, h_4 = 0 MPa/°C, $h_5 - 1.4 \times 10^{-3}$ $MPa/°C^2$

For $T > 304°C$

h_3 = 568.0 MPa, h_4 = -0.6 MPa/°C, h_5 = 0 $MPa/°C^2$

Table 3 Thermo-Mechanical Test Summary

Figure No.	T_{min}(°C)	T_{max}(°C)	$\dot{T}_{heat}$ (°C/sec)	$\dot{T}_{cool}$(°C/sec)
34	150	600	12.0	-3.5
35	150	600	12.0	-3.5
36	150	450	10.0	-5.0
37	150	400	10.0	-5.0
38	400	700	11.5	-8.0
39	400	600	9.0	-7.0
40	500	700	11.5	-7.5
41	500	600	11.5	-7.0

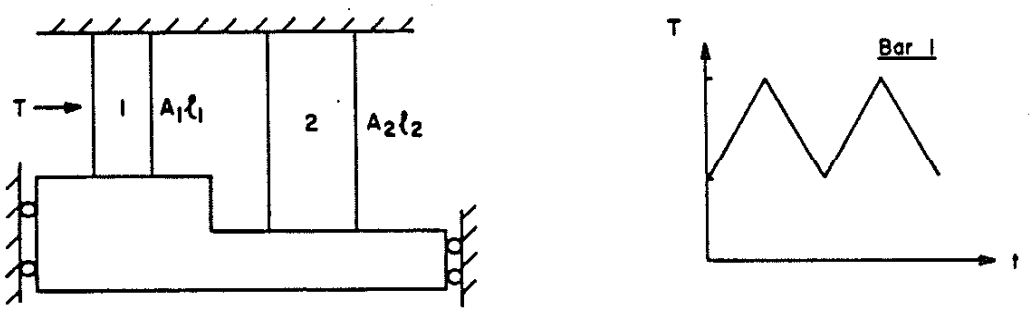

(a) Total and Partial Constraint

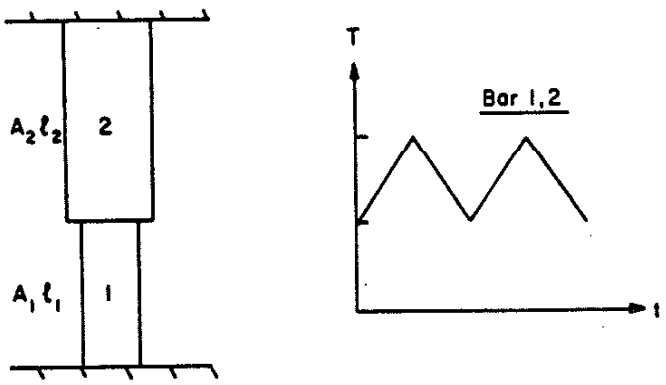

(b) Over Constraint

Figure 1 Two Bar Model Schematic

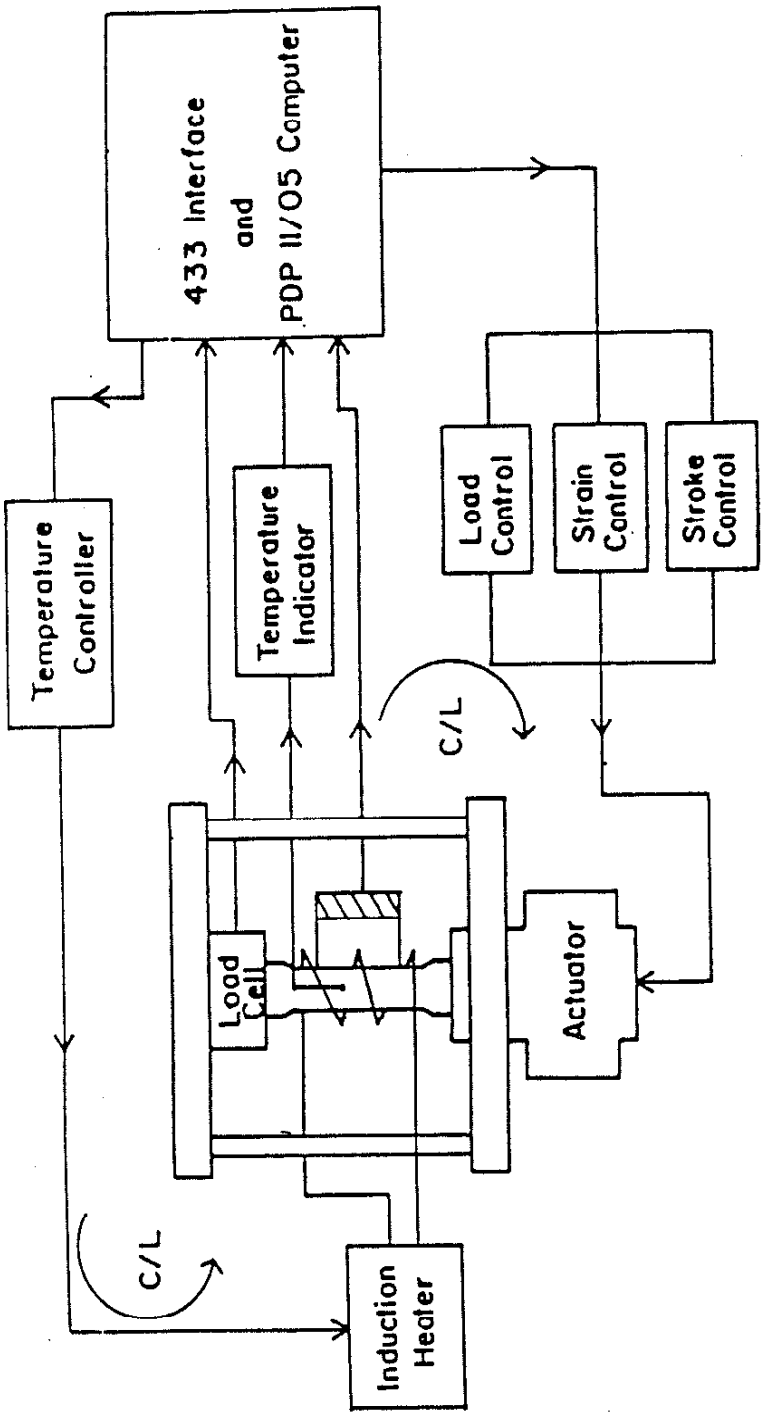

Figure 2 Test System Schematic

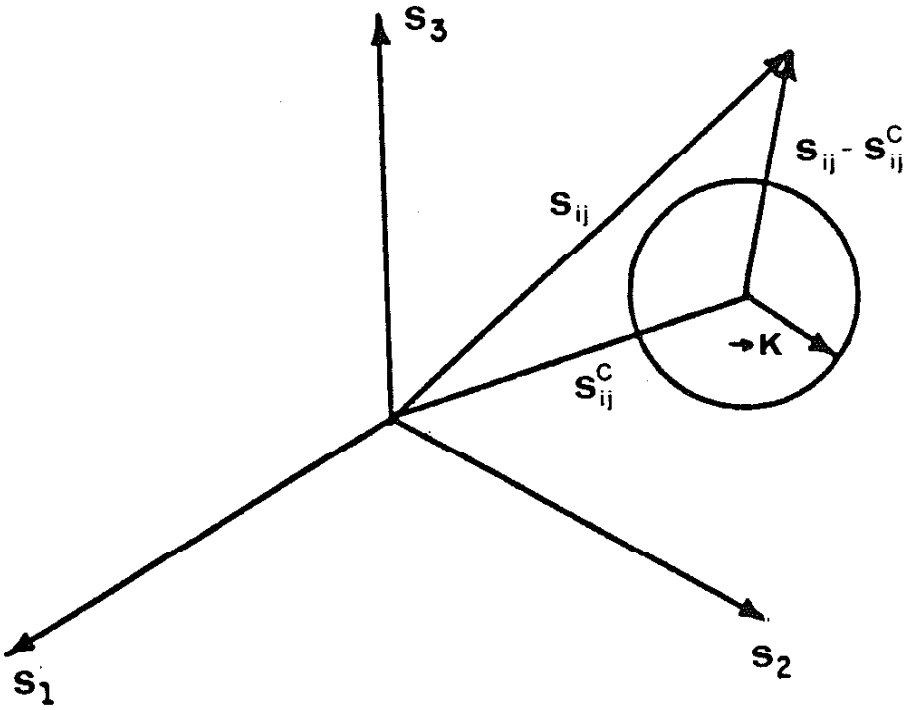

Figure 3 State Representation in Deviatoric Stress Space

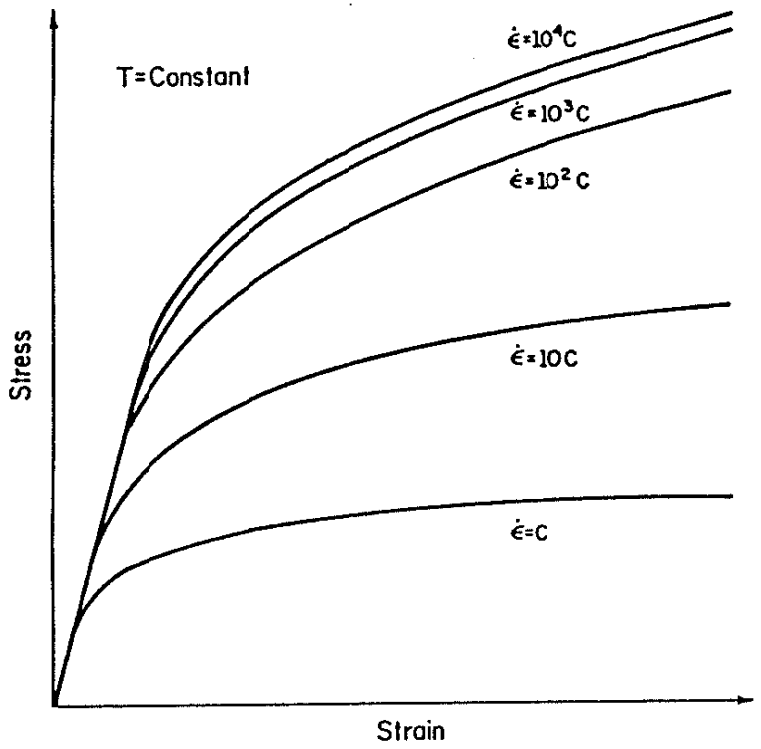

(a) Strain Rate Dependence of the Stress-Strain Response

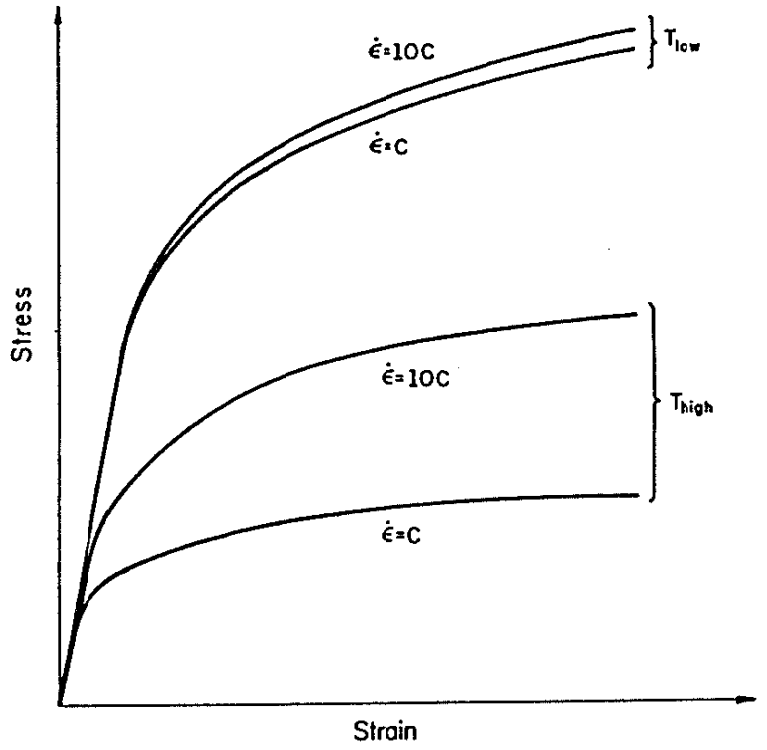

(b) Temperature and Strain Rate Dependence of the Stress-Strain Response

Figure 4 Strain Rate Sensitivity Schematic

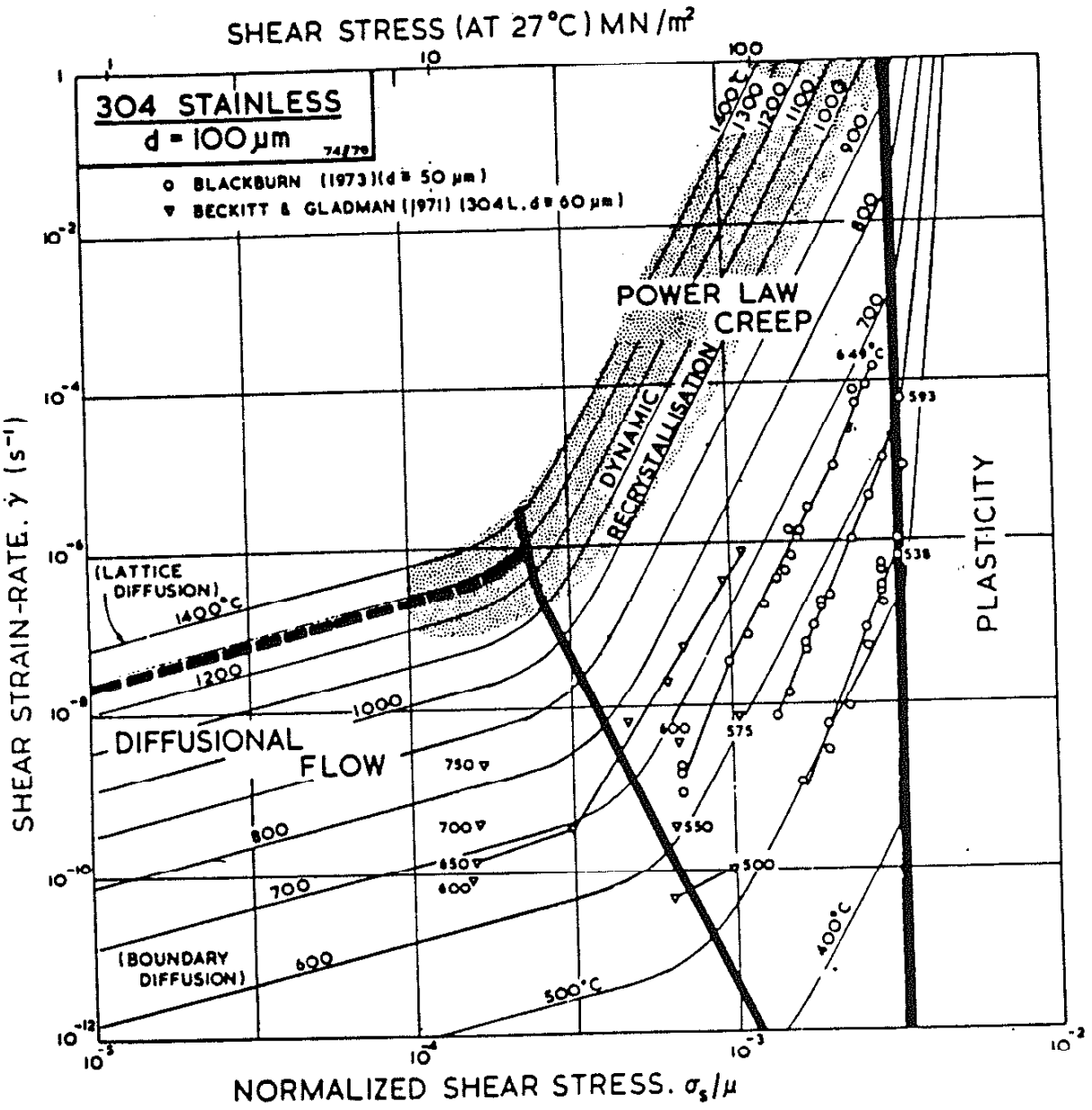

Figure 5 Deformation Mechanism Map for 304 Stainless Steel [24]

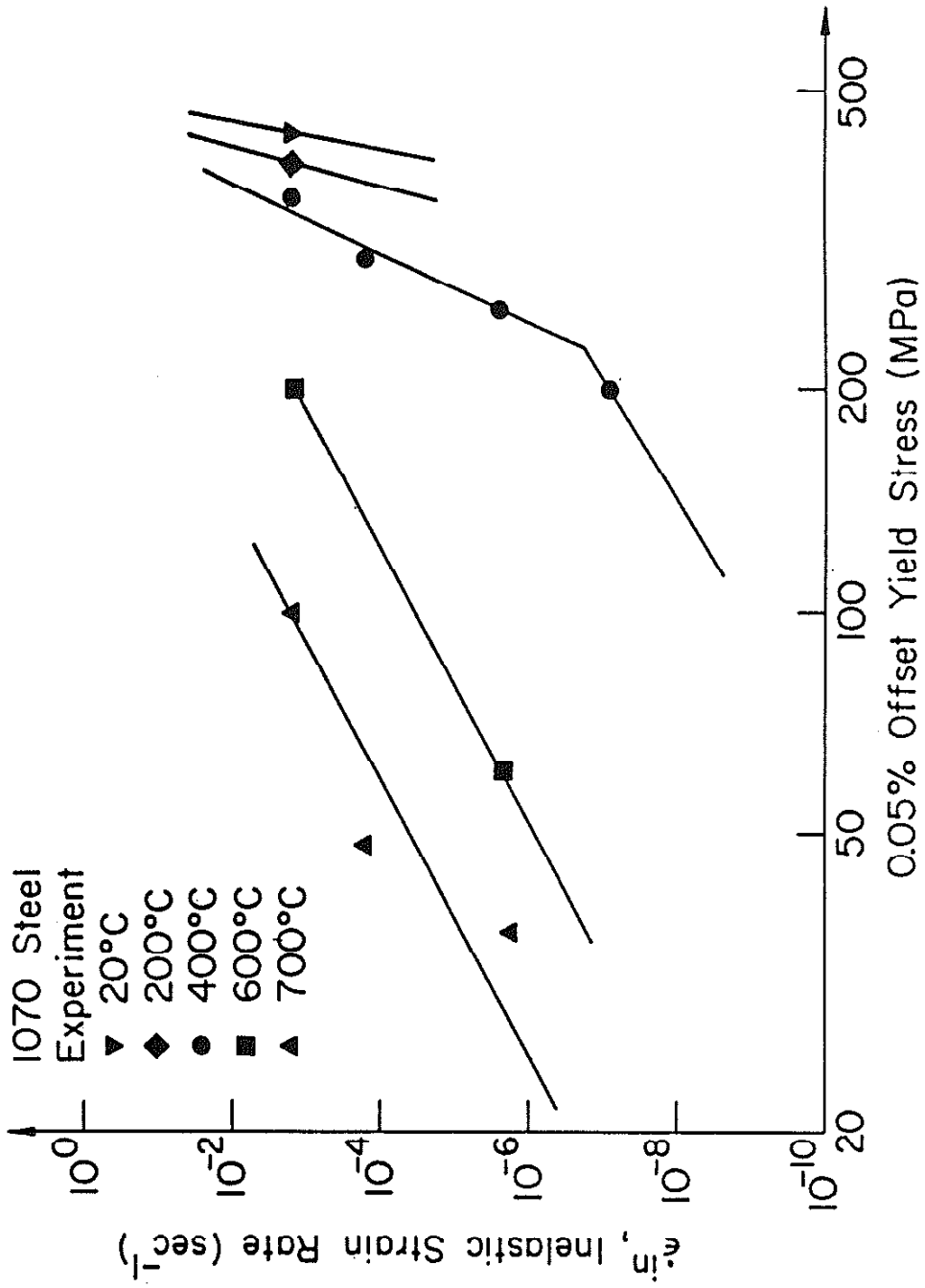

Figure 6 Offset Yield Stress Measurements

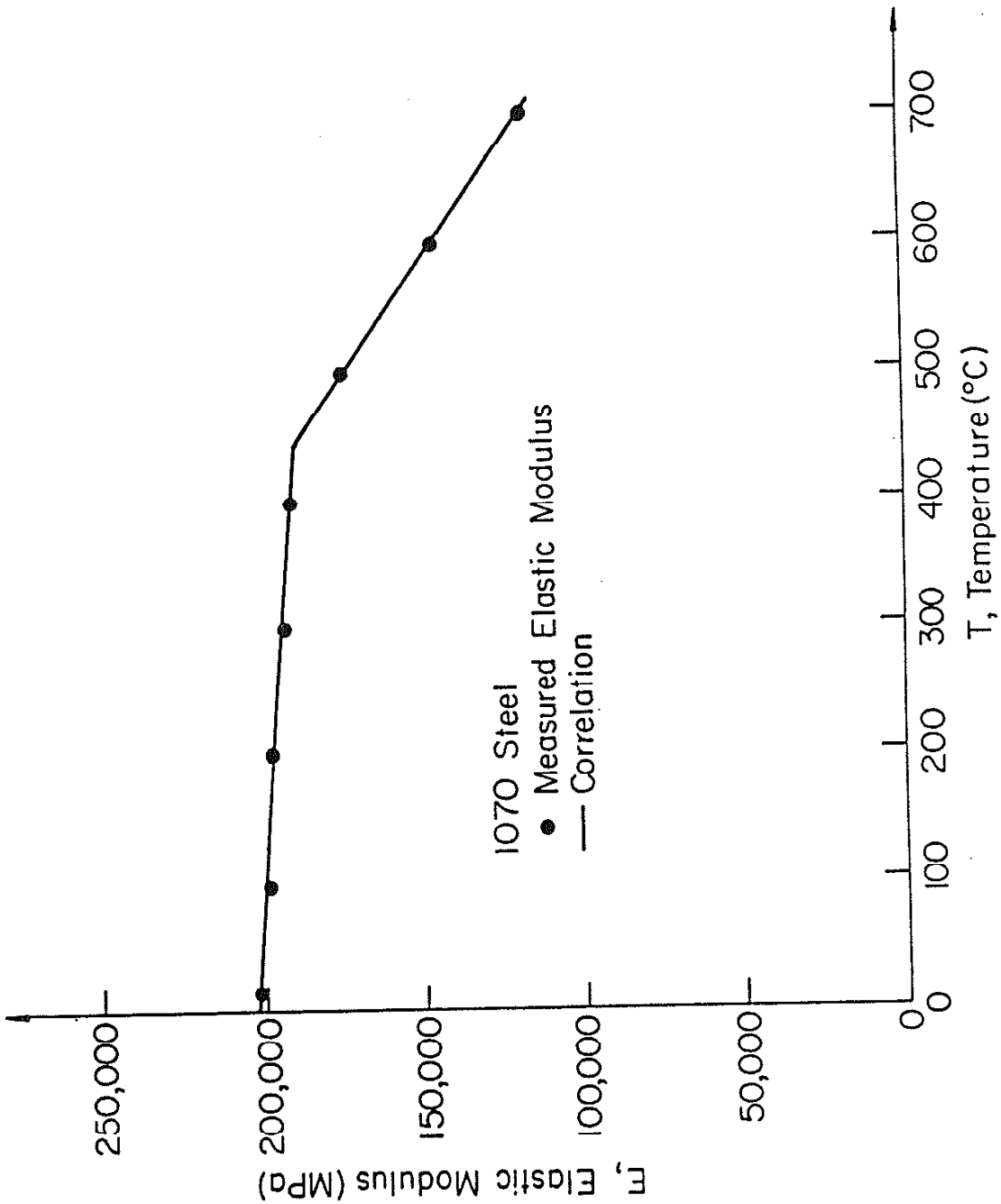

Figure 7 The Elastic Modulus, E, as a Function of Temperature

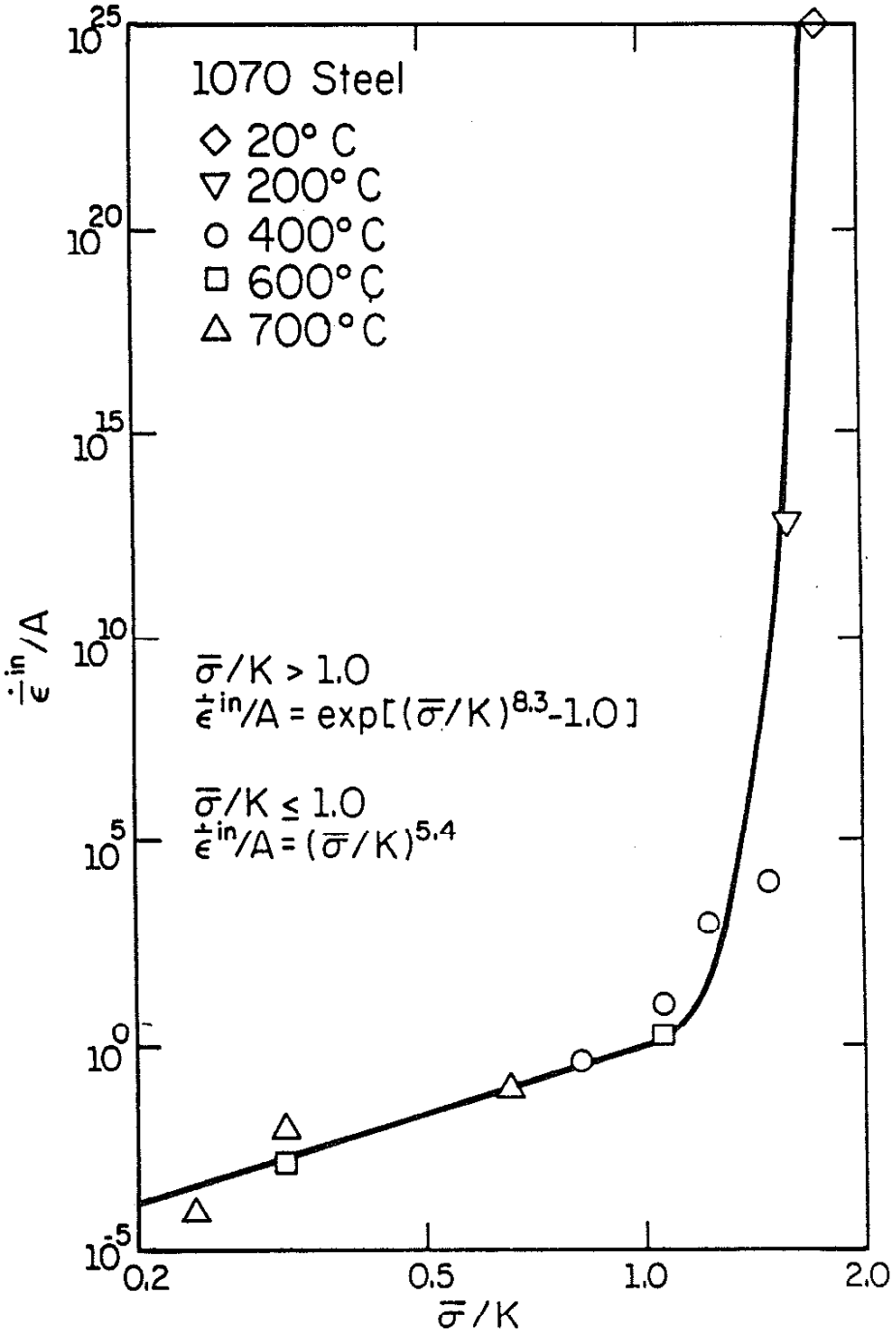

Figure 8 Experimental Determination of the Flow Rule

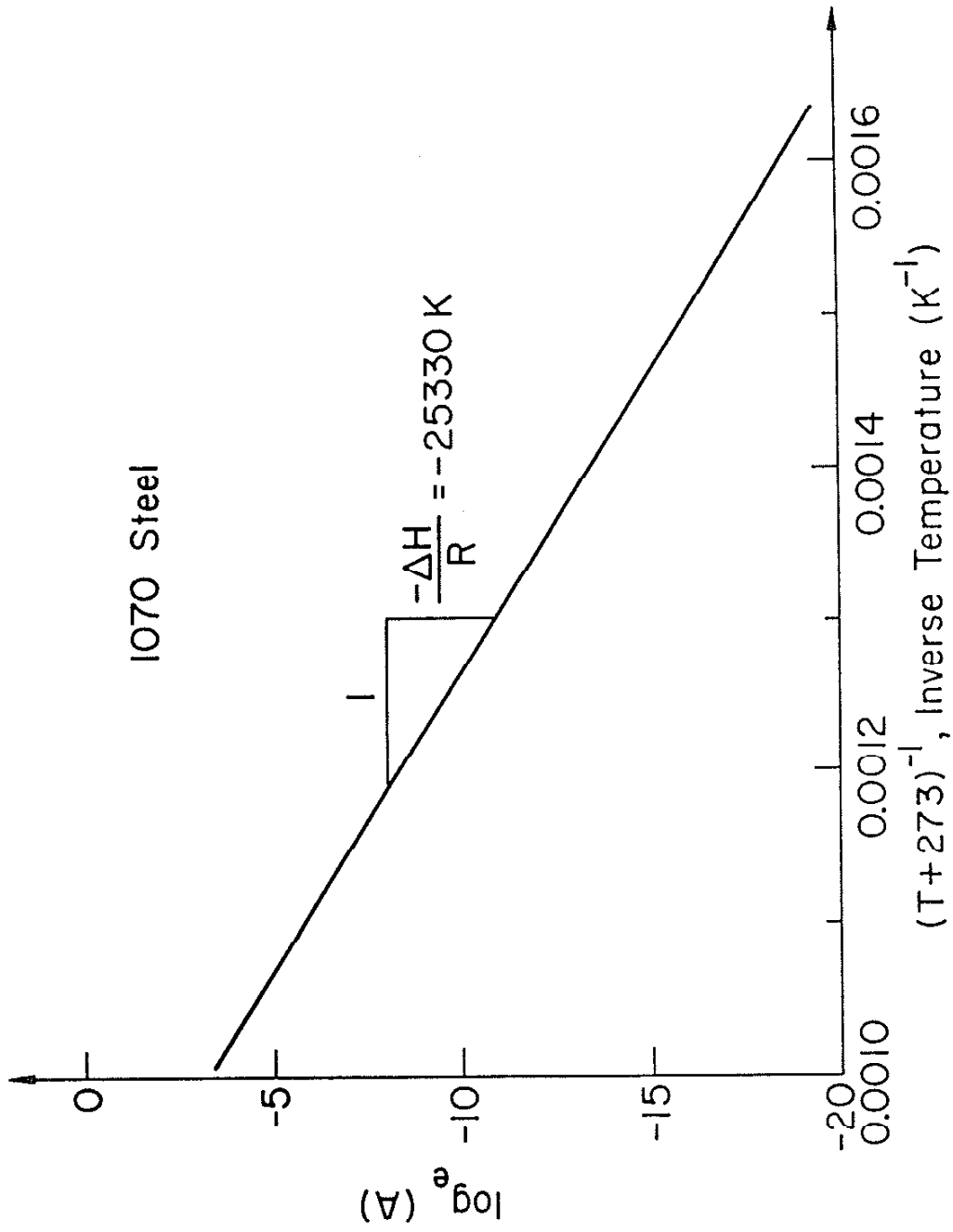

Figure 9 Determination of the Flow Rule Constant "A"

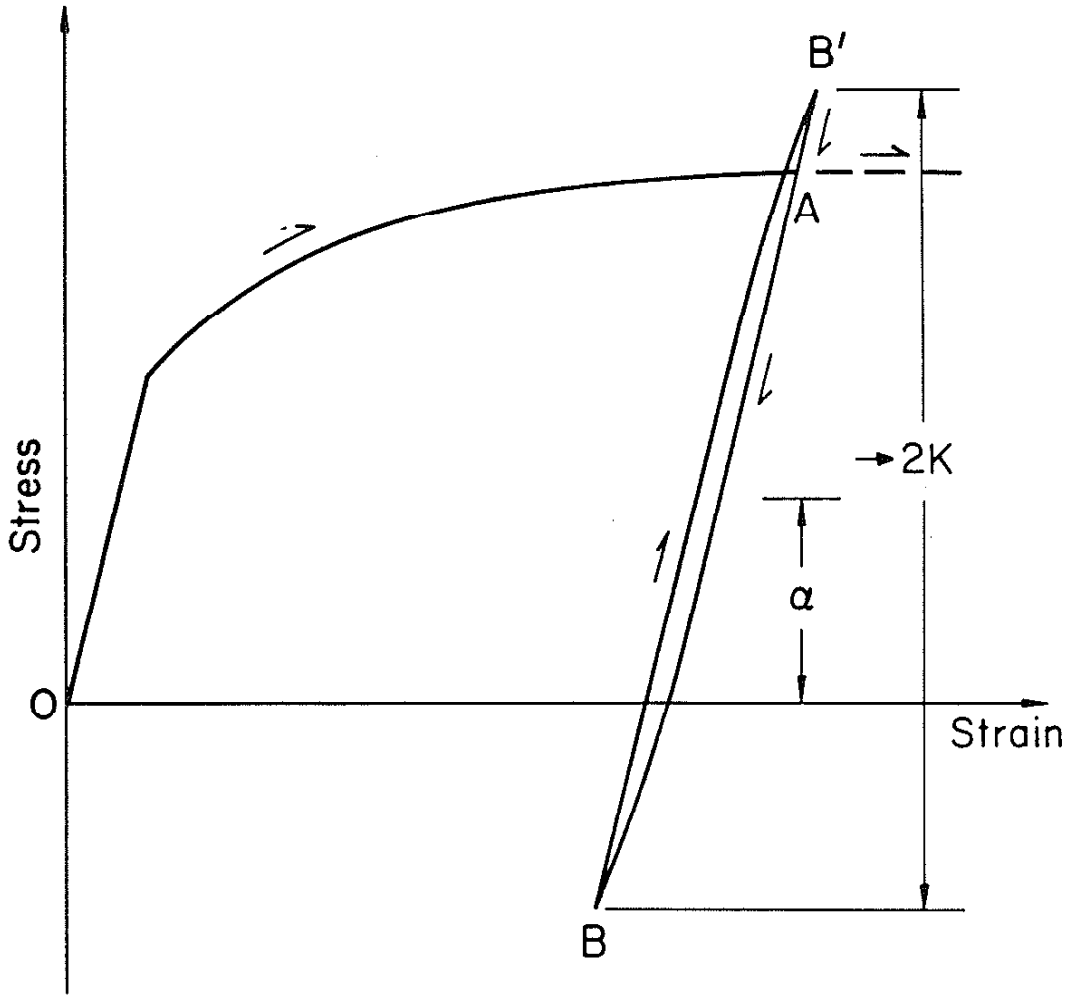

Figure 10 Internal State Measurement Technique with a Rapid Unloading-Reloading Cycle

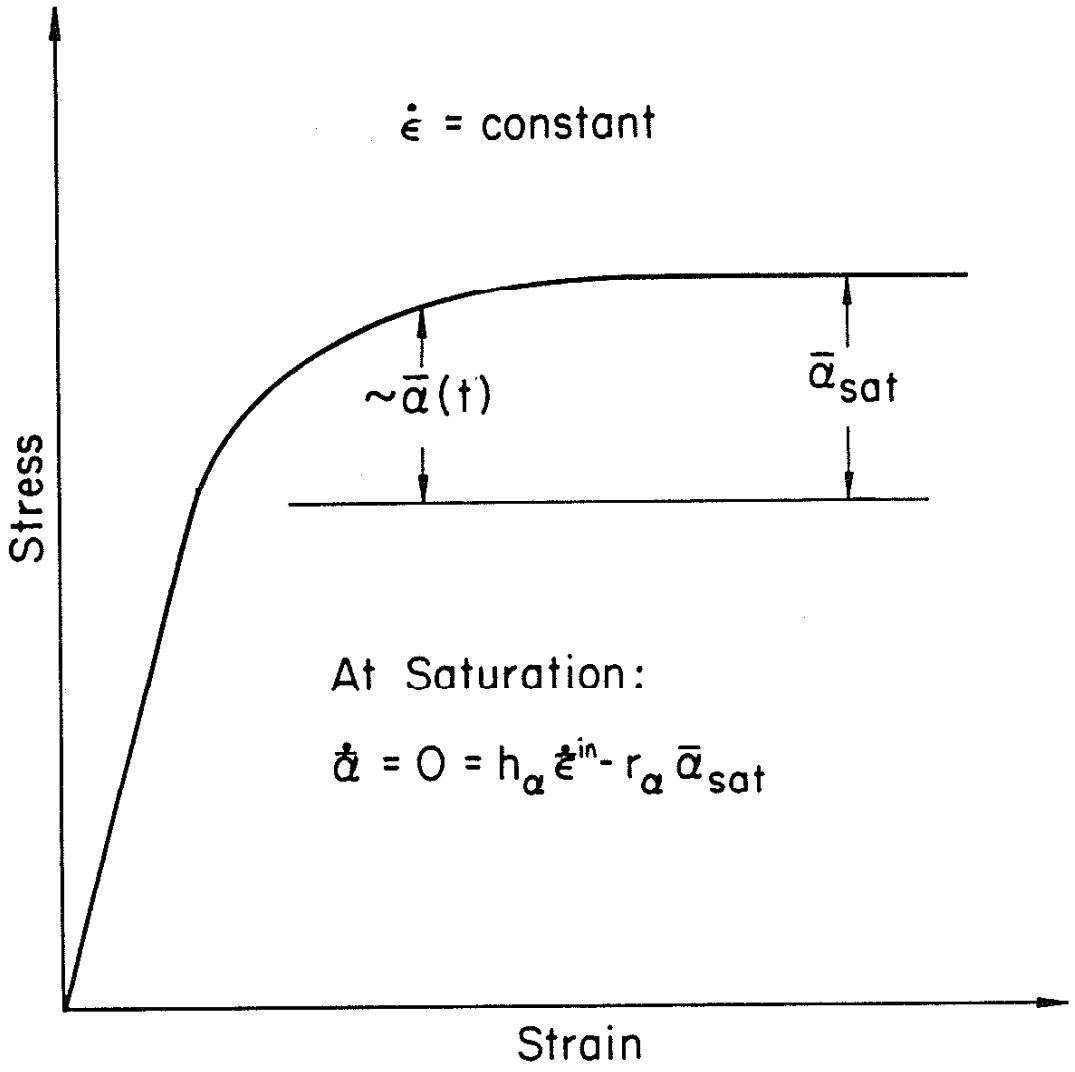

Figure 11 Measurement Technique for the Evolution of the Back Stress

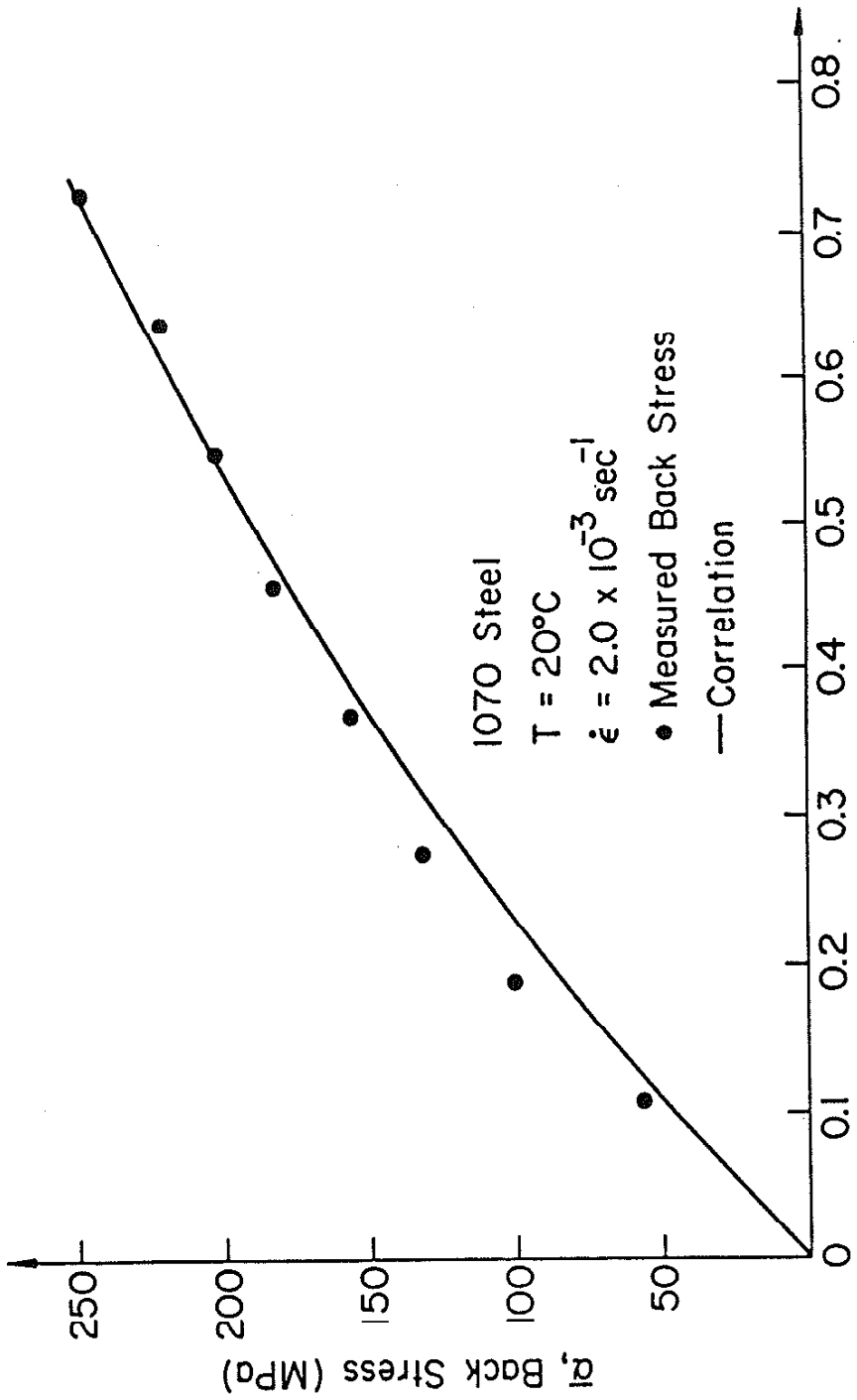

Figure 12 Experimental Determination of the Back Stress Hardening Function, h_α, Based on Low Temperature Material Response

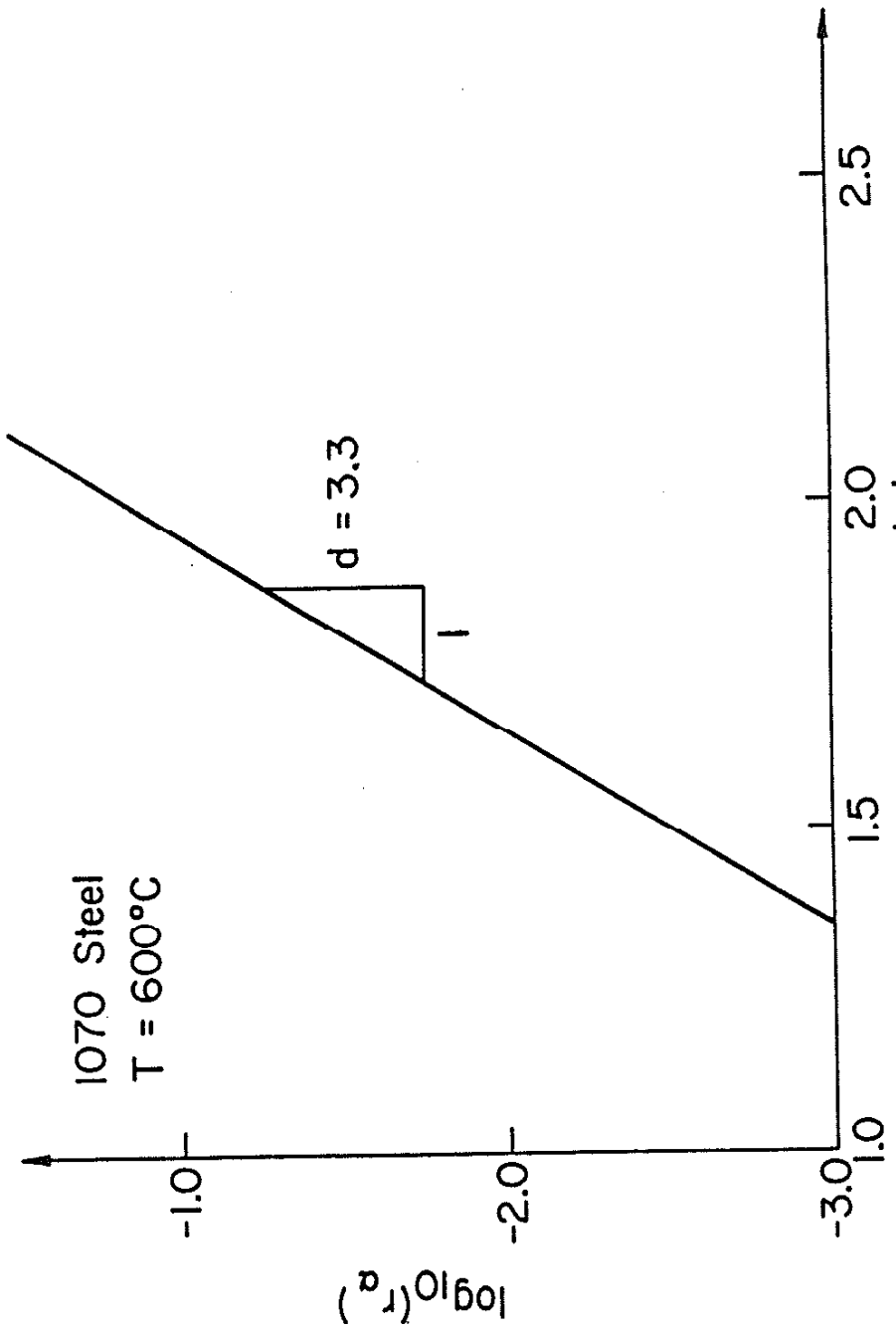

(a) The Back Stress Recovery Exponent, d

Figure 13 Experimental Determination of the Back Stress Recovery Function, r_α, Based on High Temperature Material Response

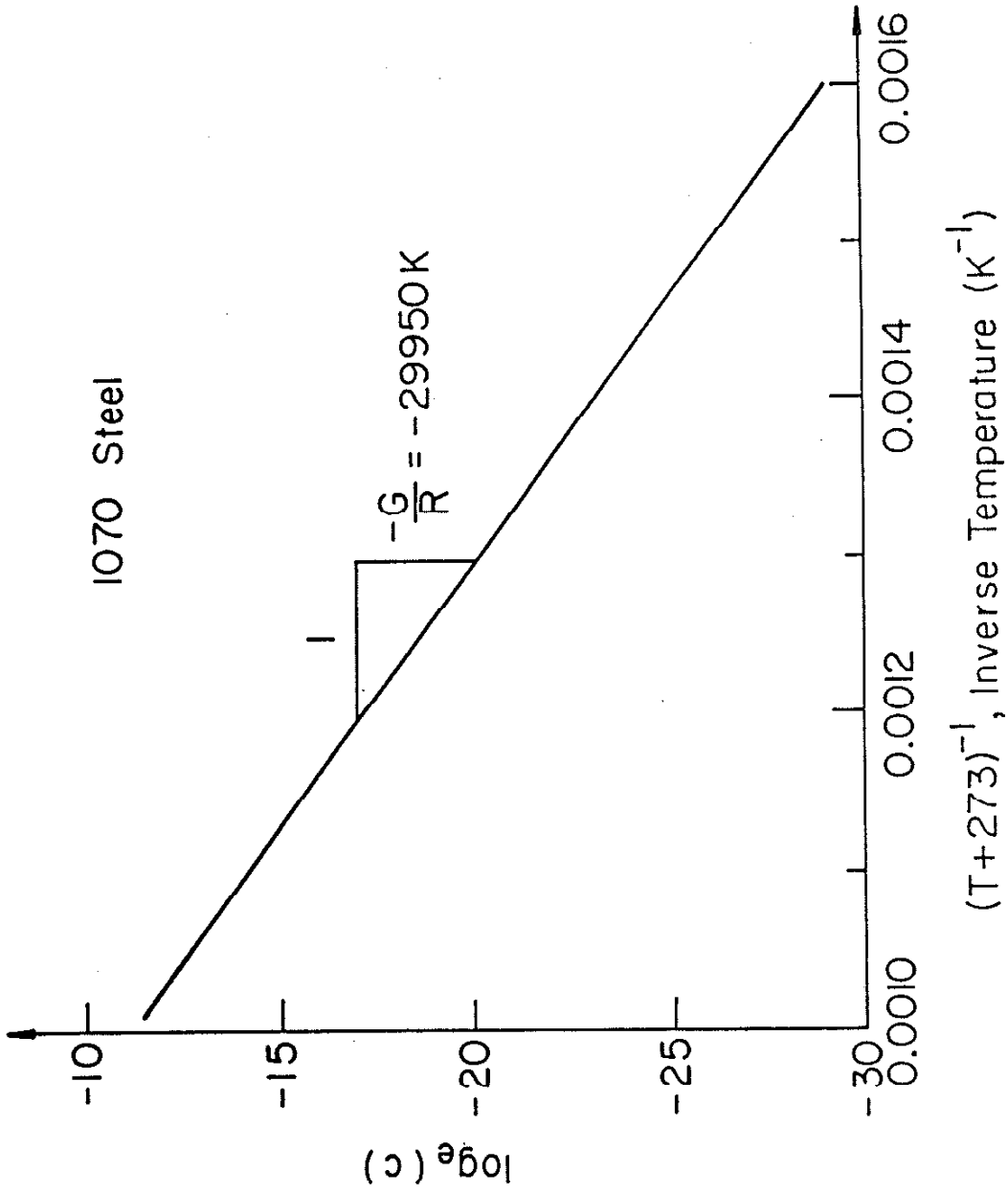

(b) The Back Stress Recovery Coefficient, c

Figure 13 (continued)

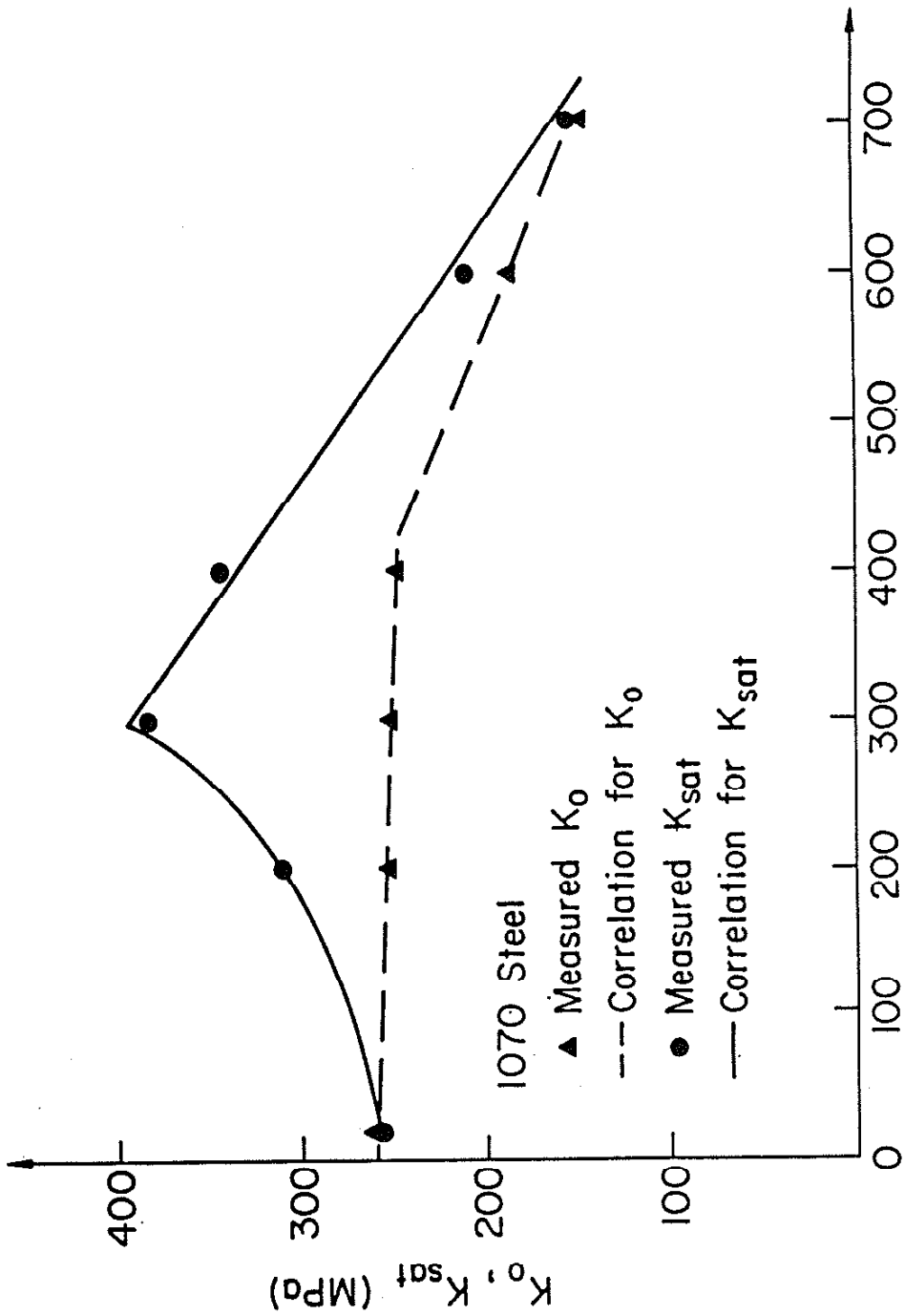

Figure 14 The Variation of the Initial Drag Stress (K_o) and the Saturated Drag Stress (K_{sat}) with Temperature

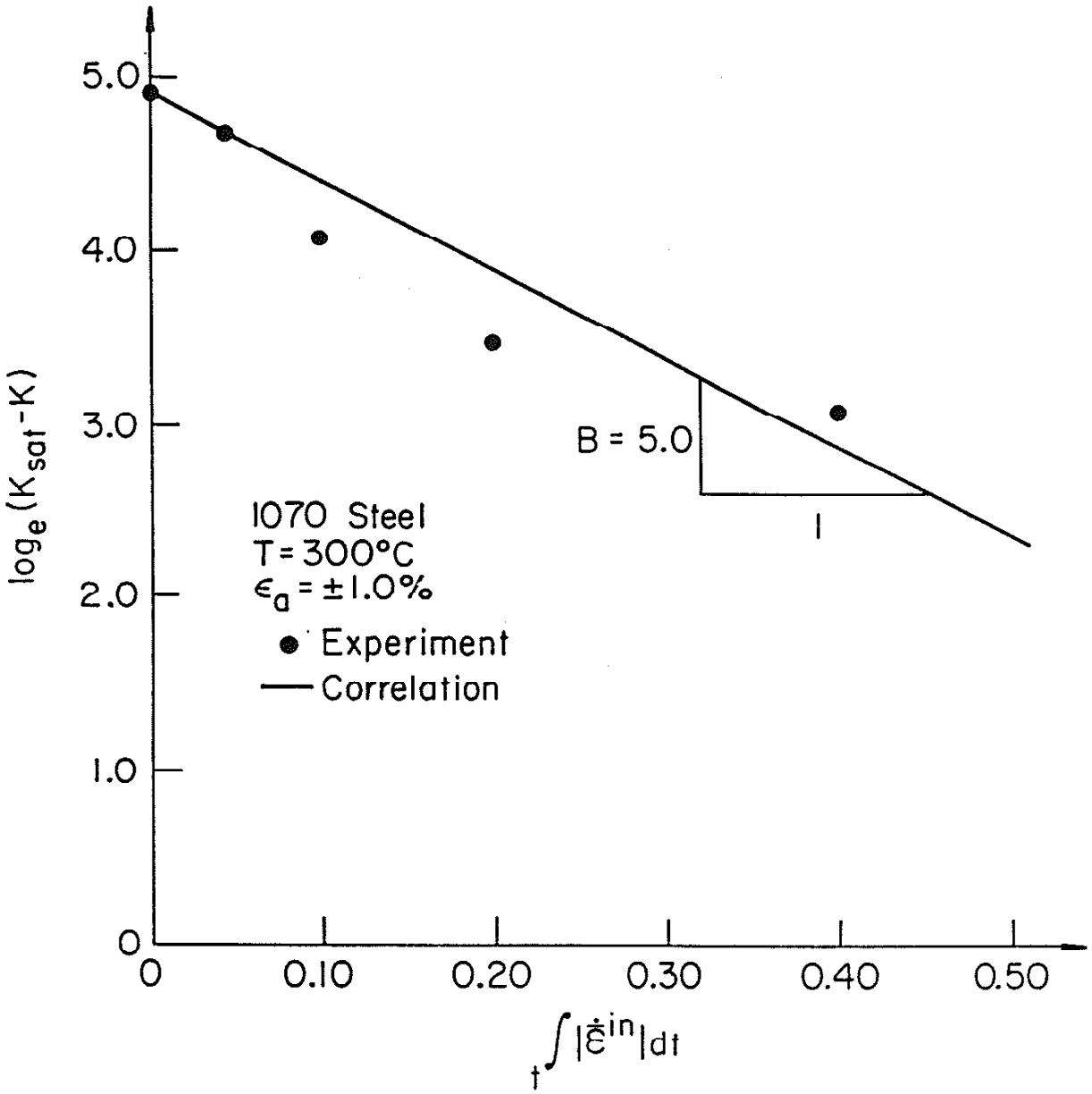

Figure 15 Determination of the Drag Stress Hardening Rate, B

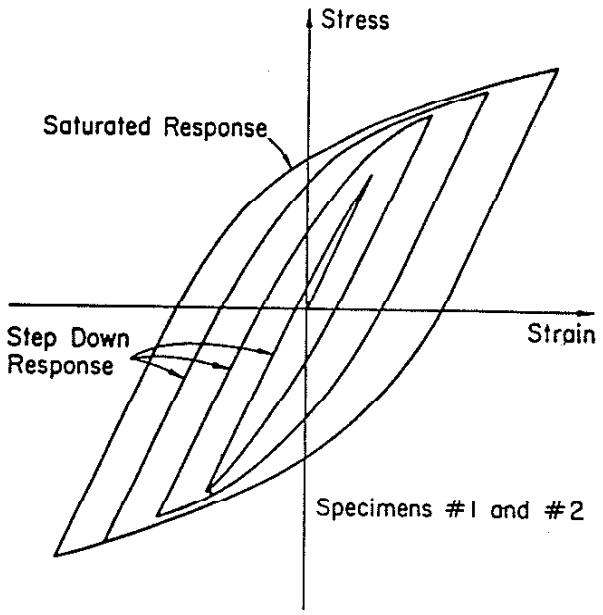

(a) Incremental Stepdown Test Stress-Strain Behavior

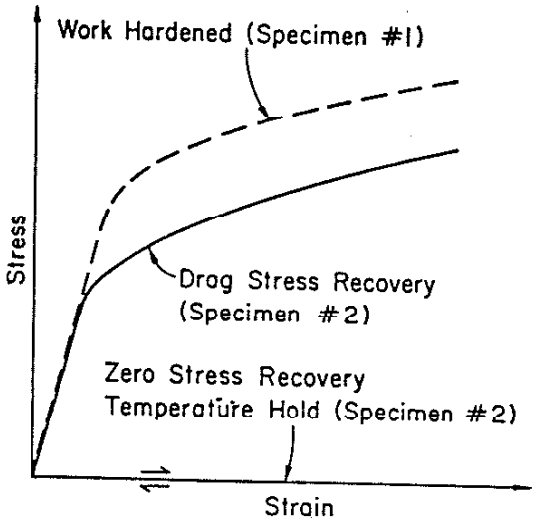

(b) Stress-Strain Behavior After Work Hardening (Specimen# 1) and after a Temperature Hold (Specimen# 2)

Figure 16 Determination of the Drag Stress Recovery Function, r_k

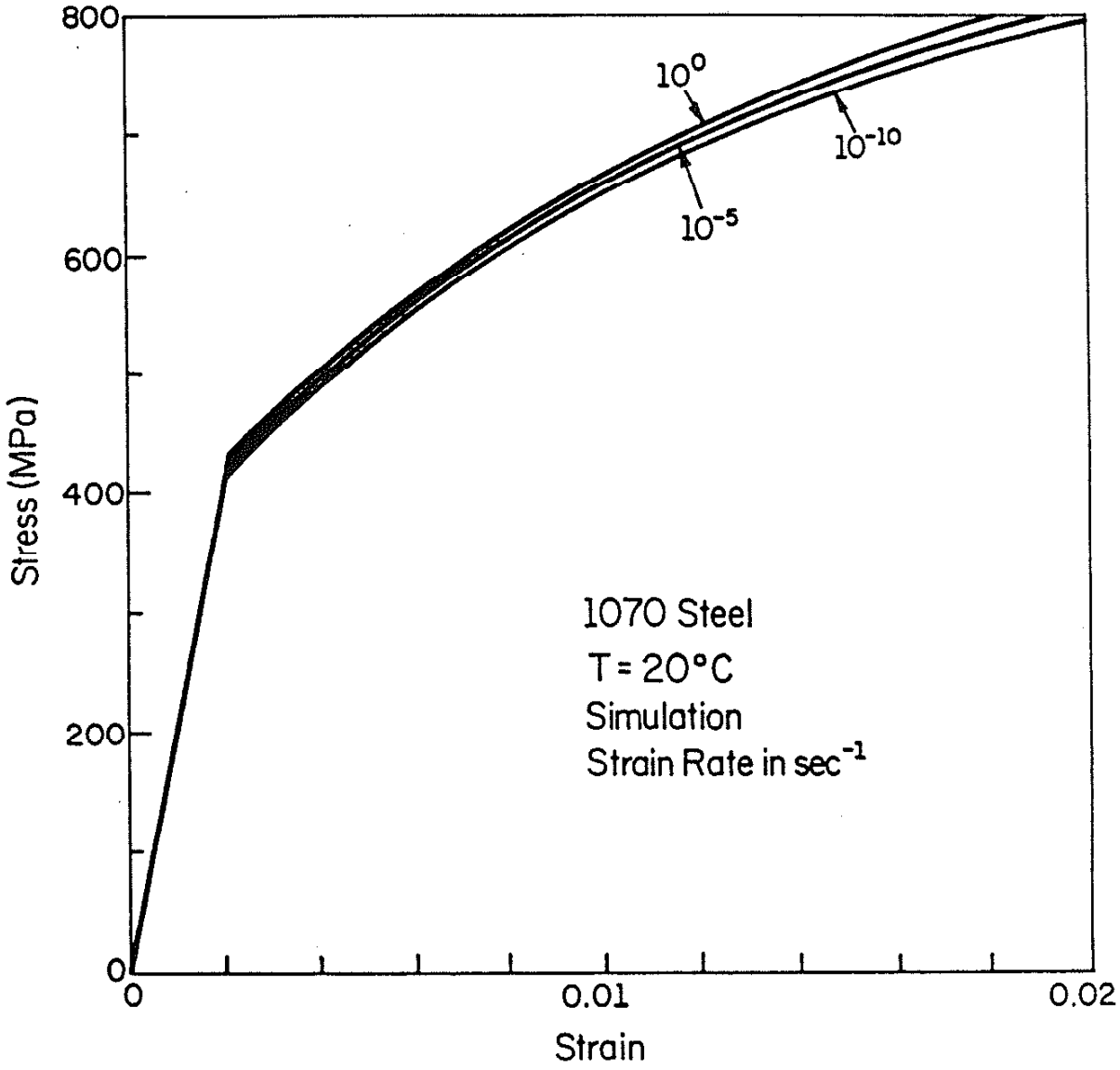

Figure 17 Strain Rate Sensitivity at 20°C

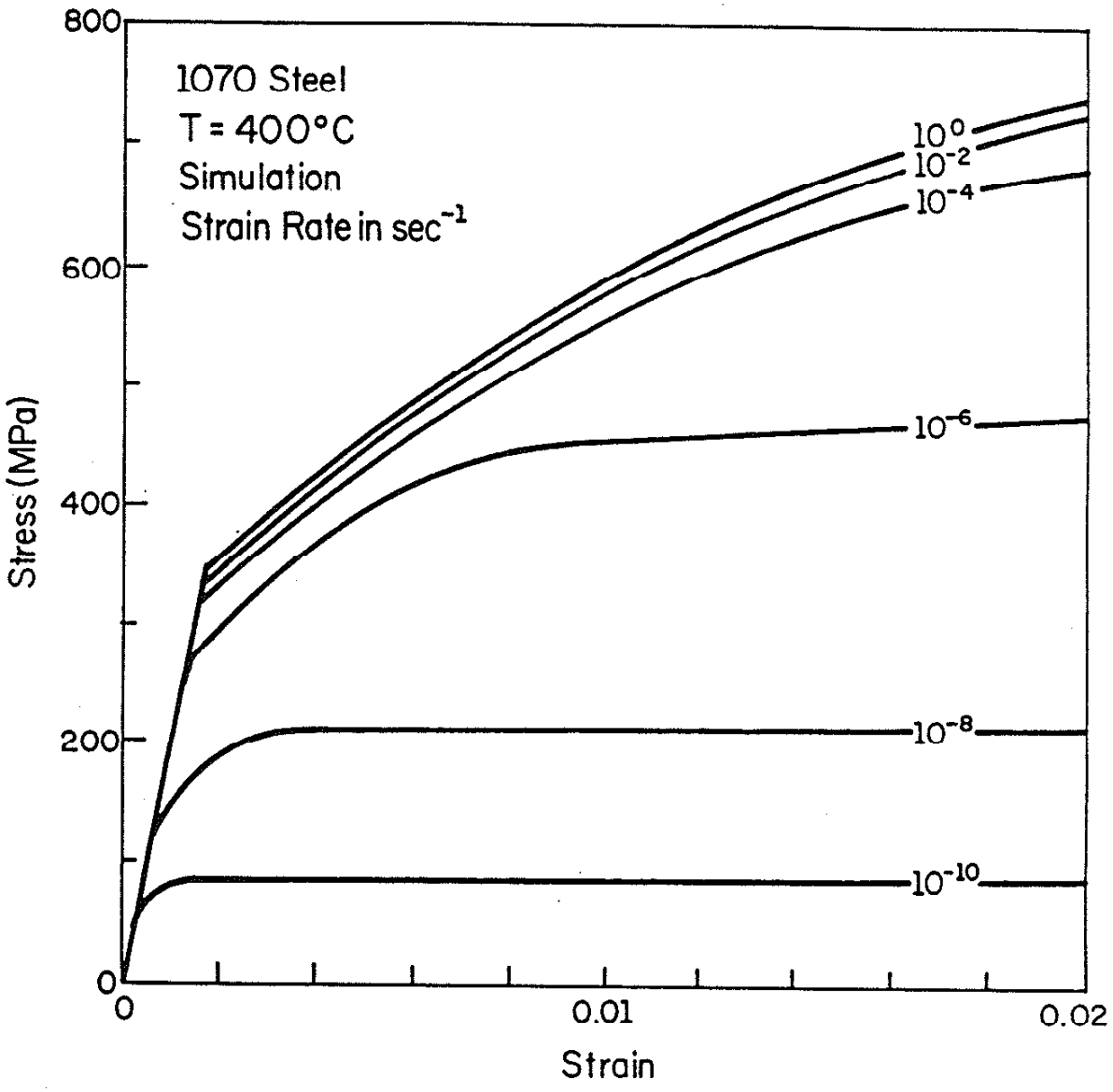

Figure 18 Strain Rate Sensitivity at 400°C

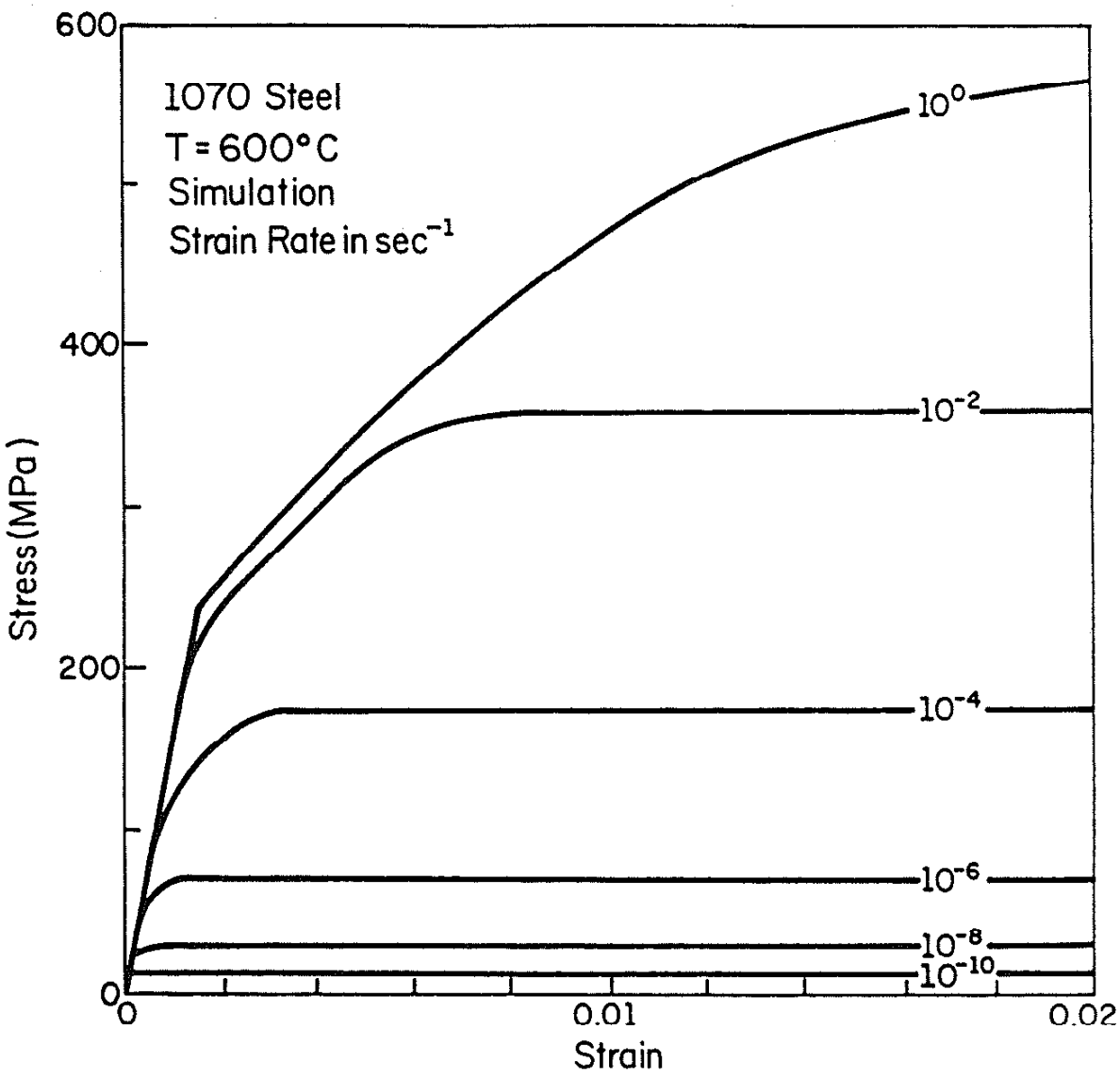

Figure 19 Strain Rate Sensitivity at 600°C

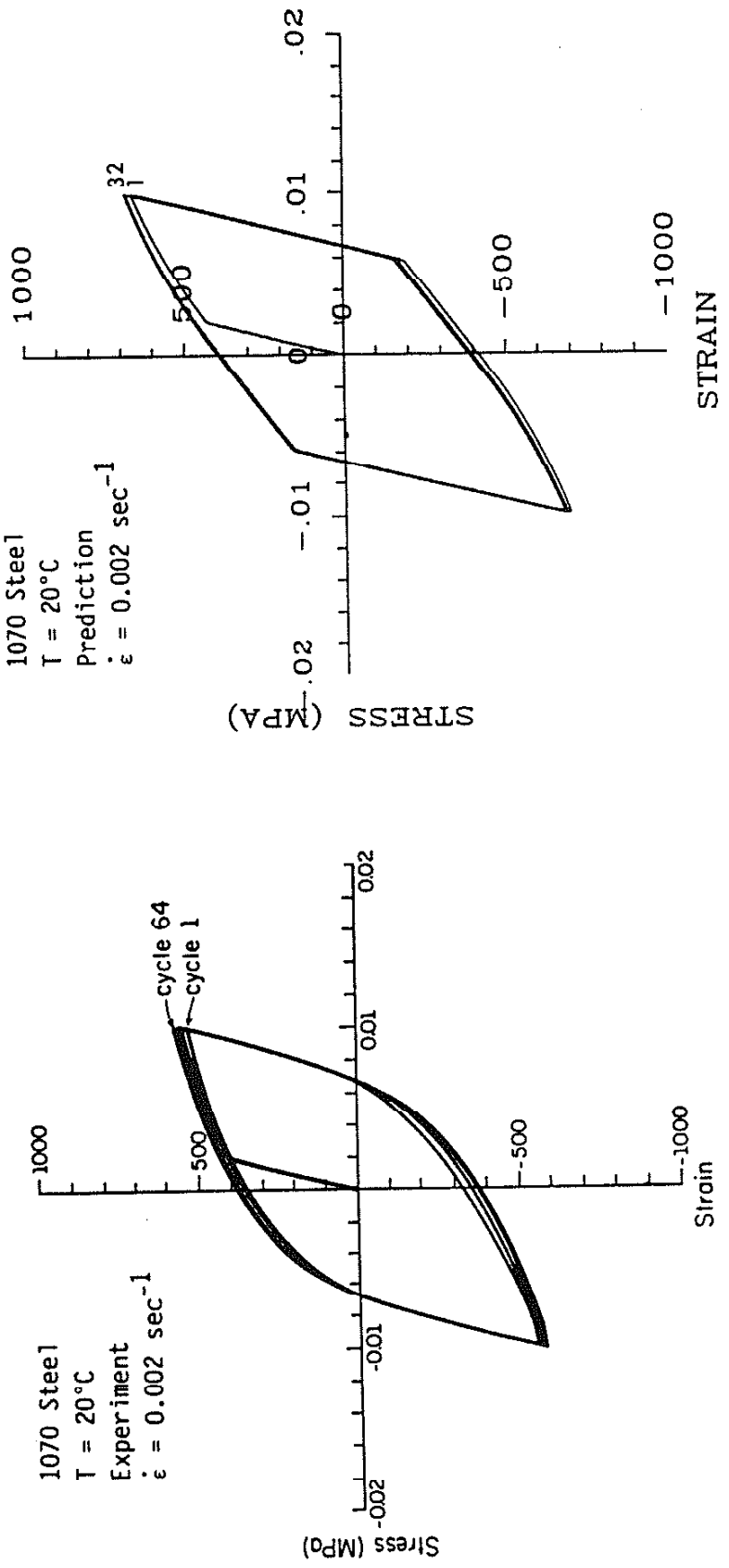

Figure 20 Comparison of Isothermal Experimental and Predicted Material Response for T = 20°C, ε_a = ±1.0%, and $\dot{\varepsilon}$ = 0.002 sec^{-1}

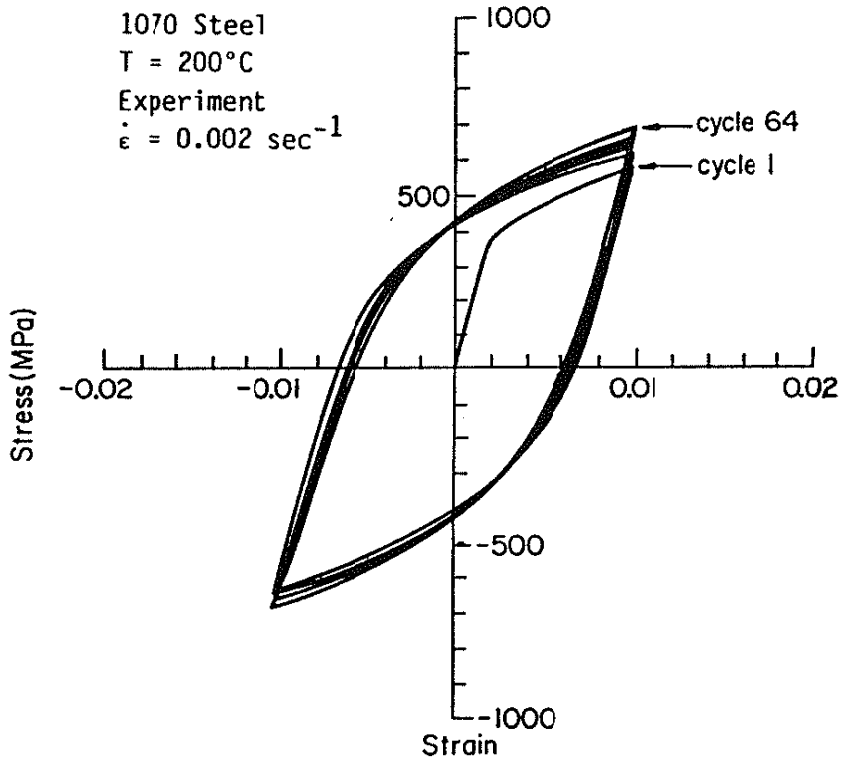

(a) Experiment

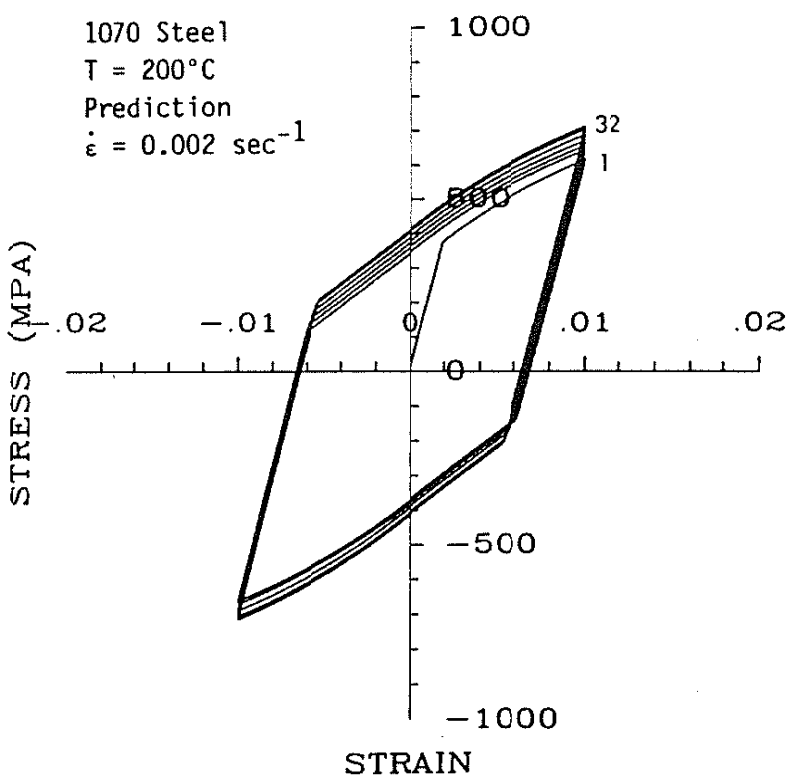

(b) Prediction

Figure 21 Comparison of Isothermal Experimental and Predicted Material Response for T = 200°C, ε_a = ±1.0%, and $\dot{\varepsilon}$ = 0.002 sec^{-1}

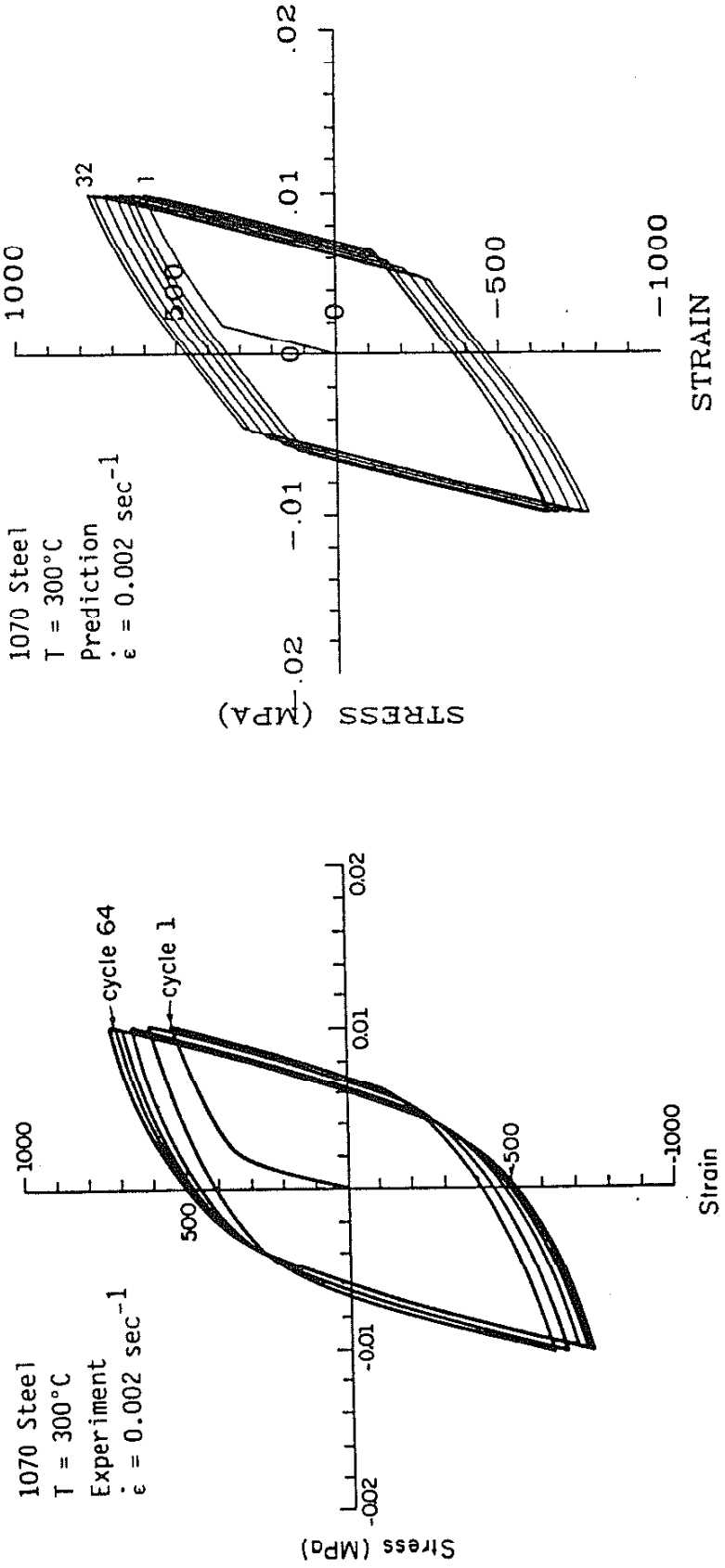

(a) Experiment

(b) Prediction

Figure 22 Comparison of Isothermal Experimental and Predicted Material Response for T = 300°C, ε_a = ±1.0%, and $\dot{\varepsilon}$ = 0.002 sec^{-1}

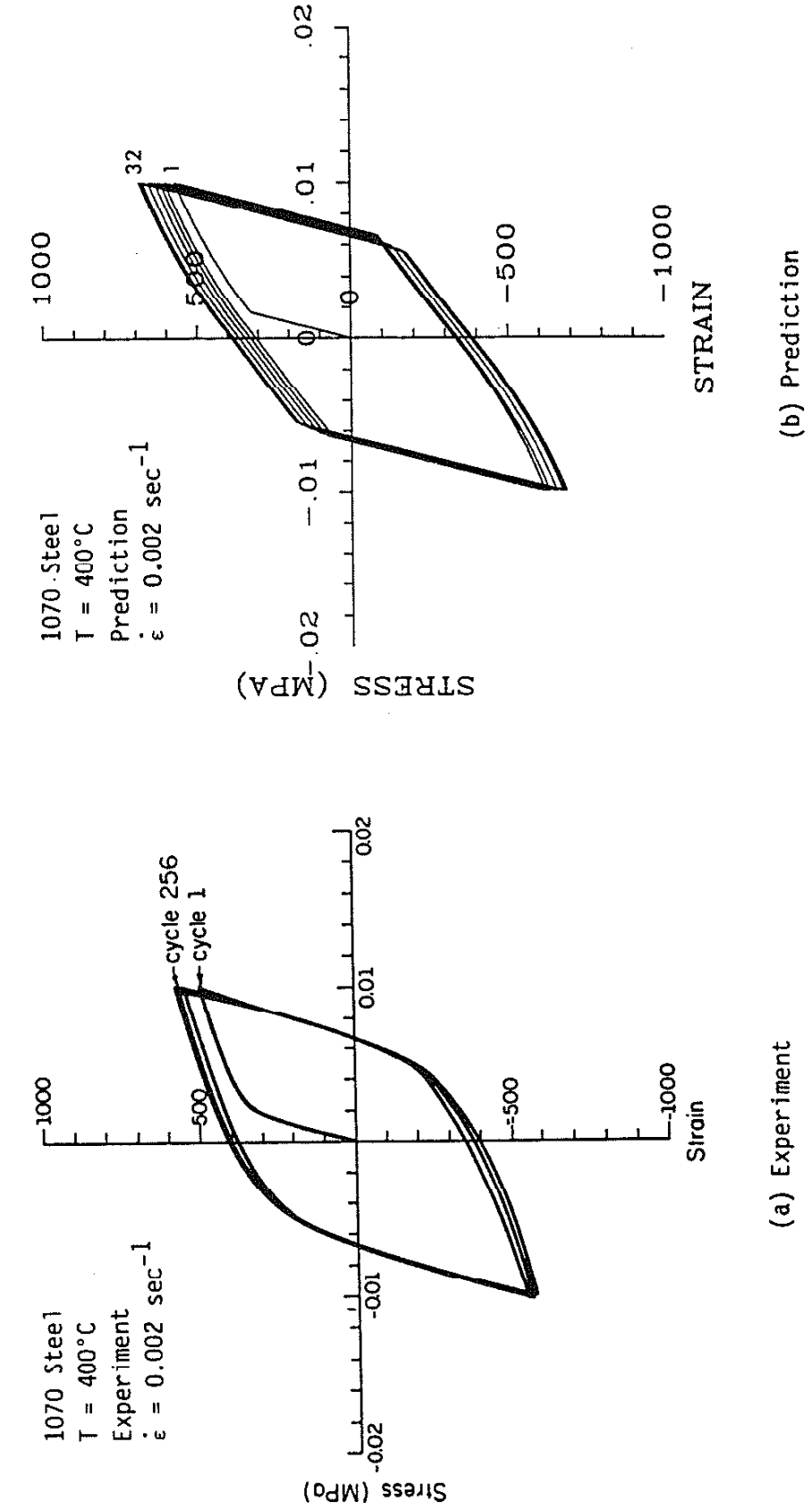

Figure 23 Comparison of Isothermal Experimental and Predicted Material Response for T = 400° C, ε_a = ±1.0%, and $\dot{\varepsilon}$ = 0.002 sec^{-1}

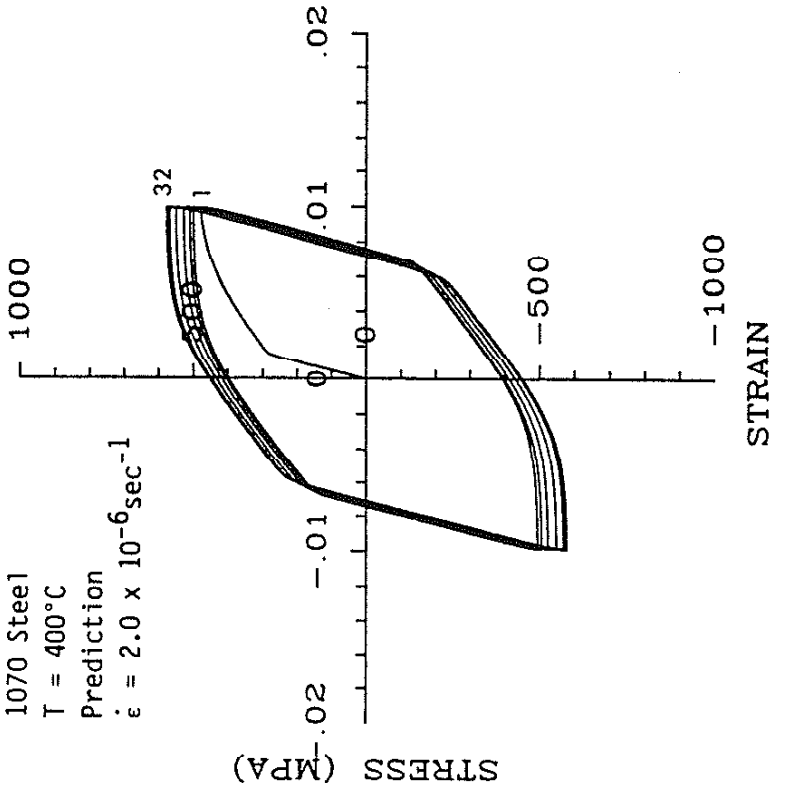

(b) Prediction

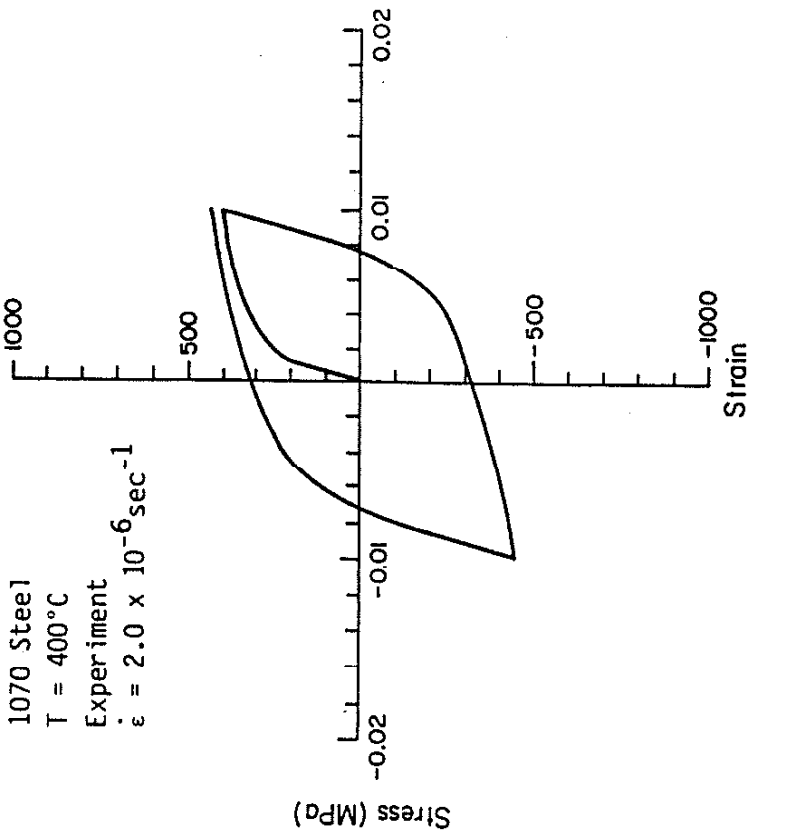

(a) Experiment

Figure 24 Comparison of Isothermal Experimental and Predicted Material Response for T = 400°C, ε_a = ±1.0%, and $\dot{\varepsilon}$ = 2.0 x 10^{-6}sec^{-1}

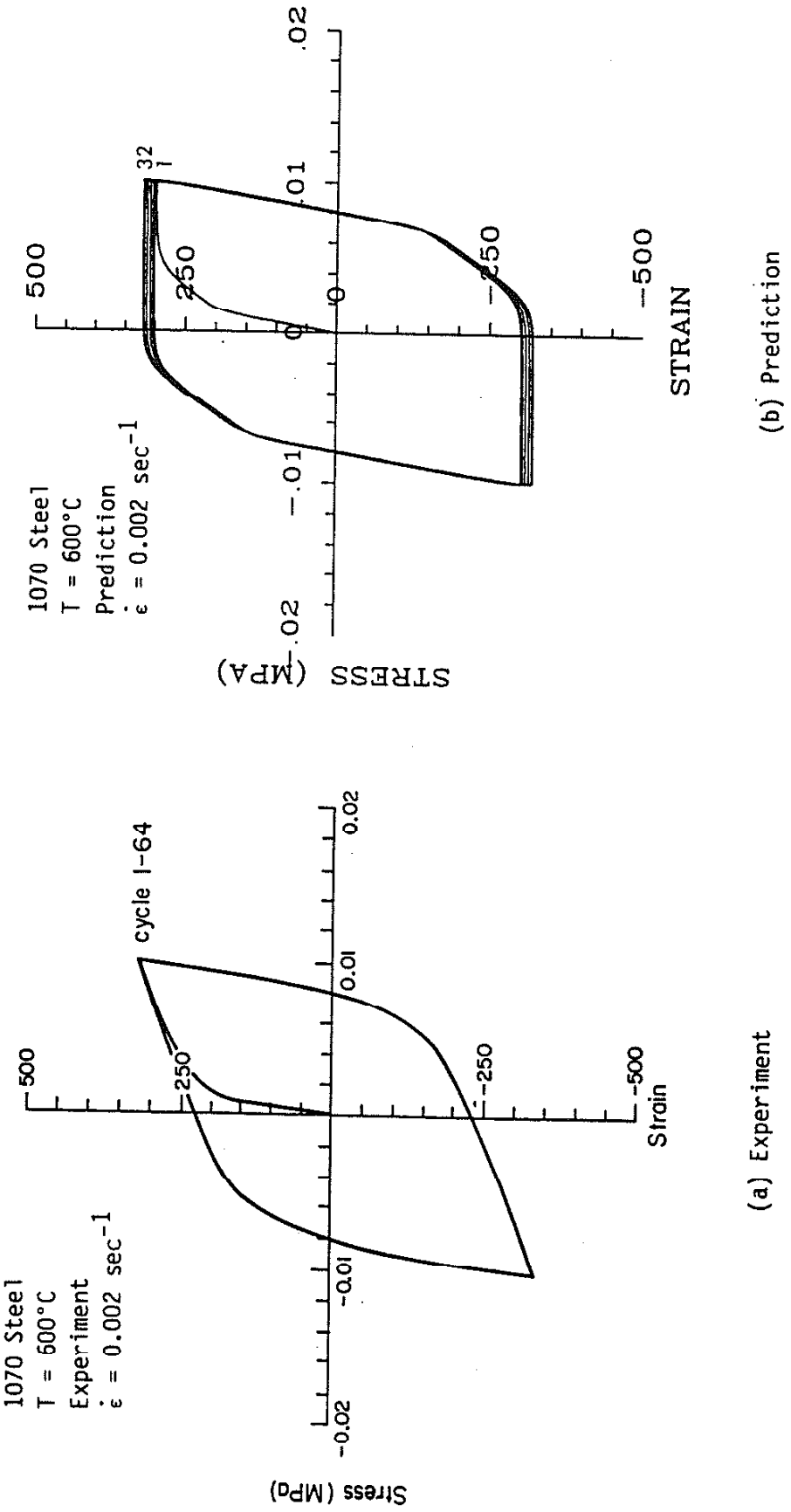

Figure 25 Comparison of Isothermal Experimental and Predicted Material Response for T = 600°C, ε_a = ±1.0%, and $\dot{\varepsilon}$ = 0.002 sec^{-1}

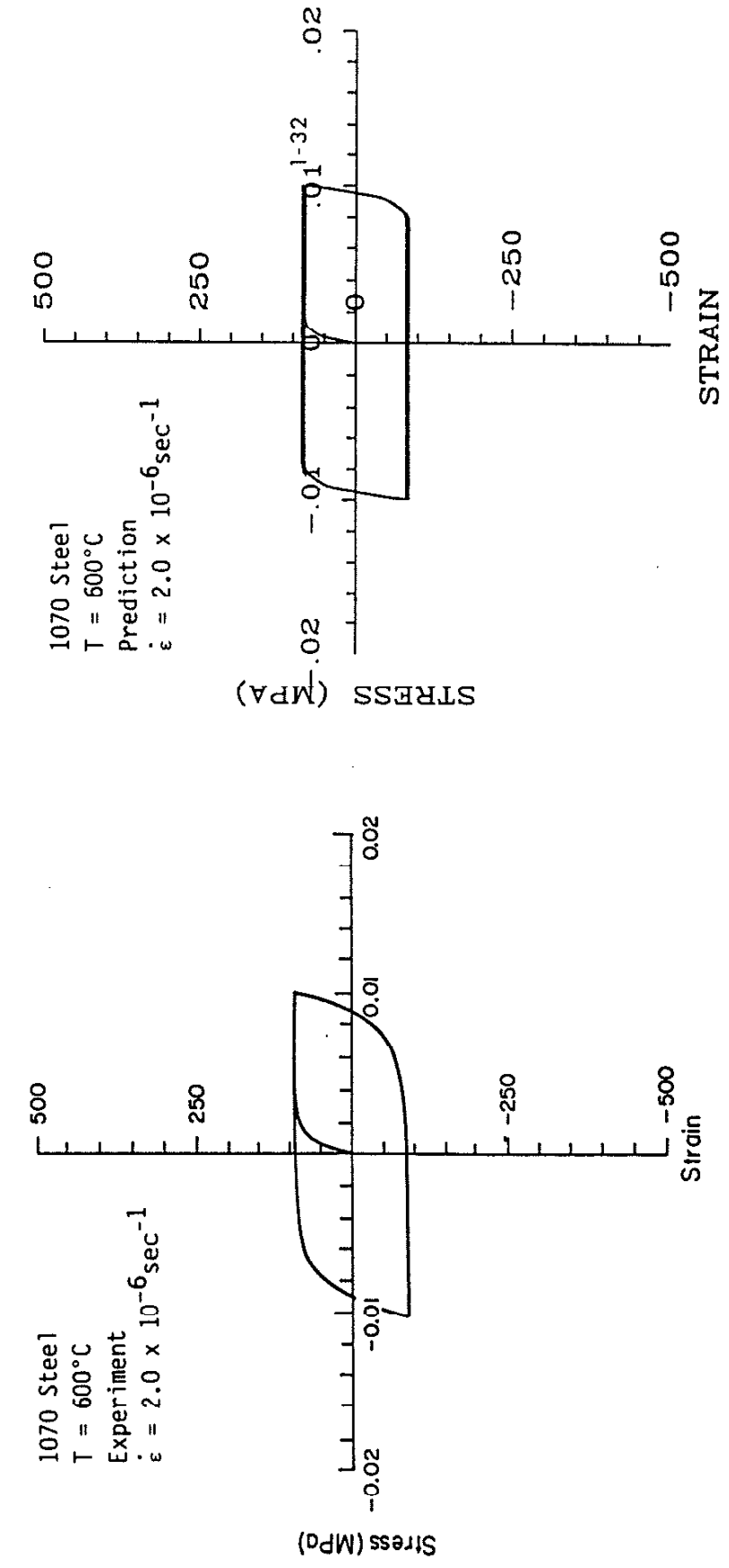

Figure 26 Comparison of Isothermal Experimental and Predicted Material Response for T = 600°C, ε_a = ±1.0%, and $\dot{\varepsilon}$ = 2.0 x 10^{-6}sec^{-1}

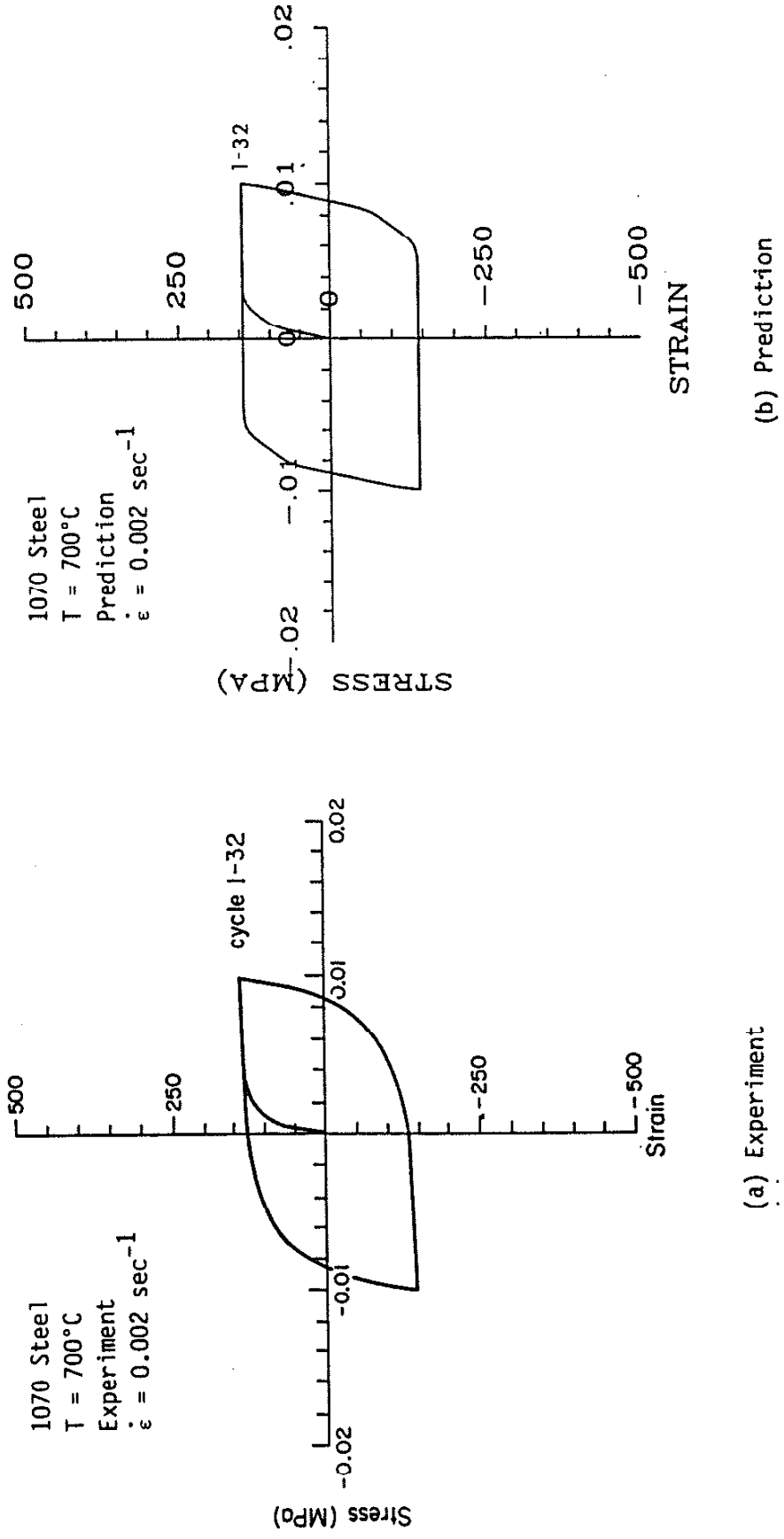

Figure 27 Comparison of Isothermal Experimental and Predicted Material Response for T = 700°C, ε_a = ±1.0%, and $\dot{\varepsilon}$ = 0.002 sec^{-1}

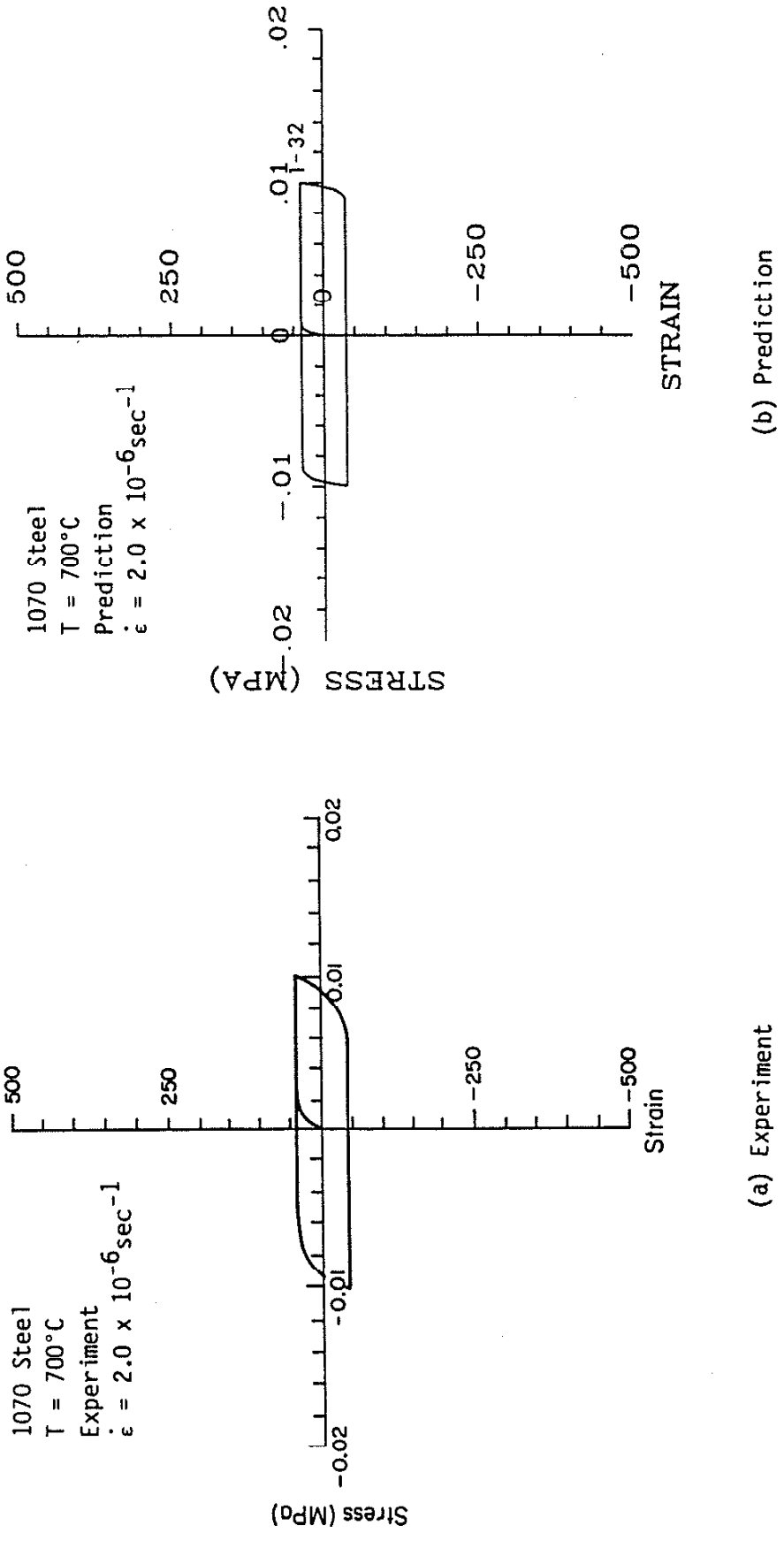

Figure 28 Comparison of Isothermal Experimental and Predicted Material Response for T = 700°C, ε_a = ±1.0%, and $\dot{\varepsilon}$ = 2.0 x 10^{-6} sec^{-1}

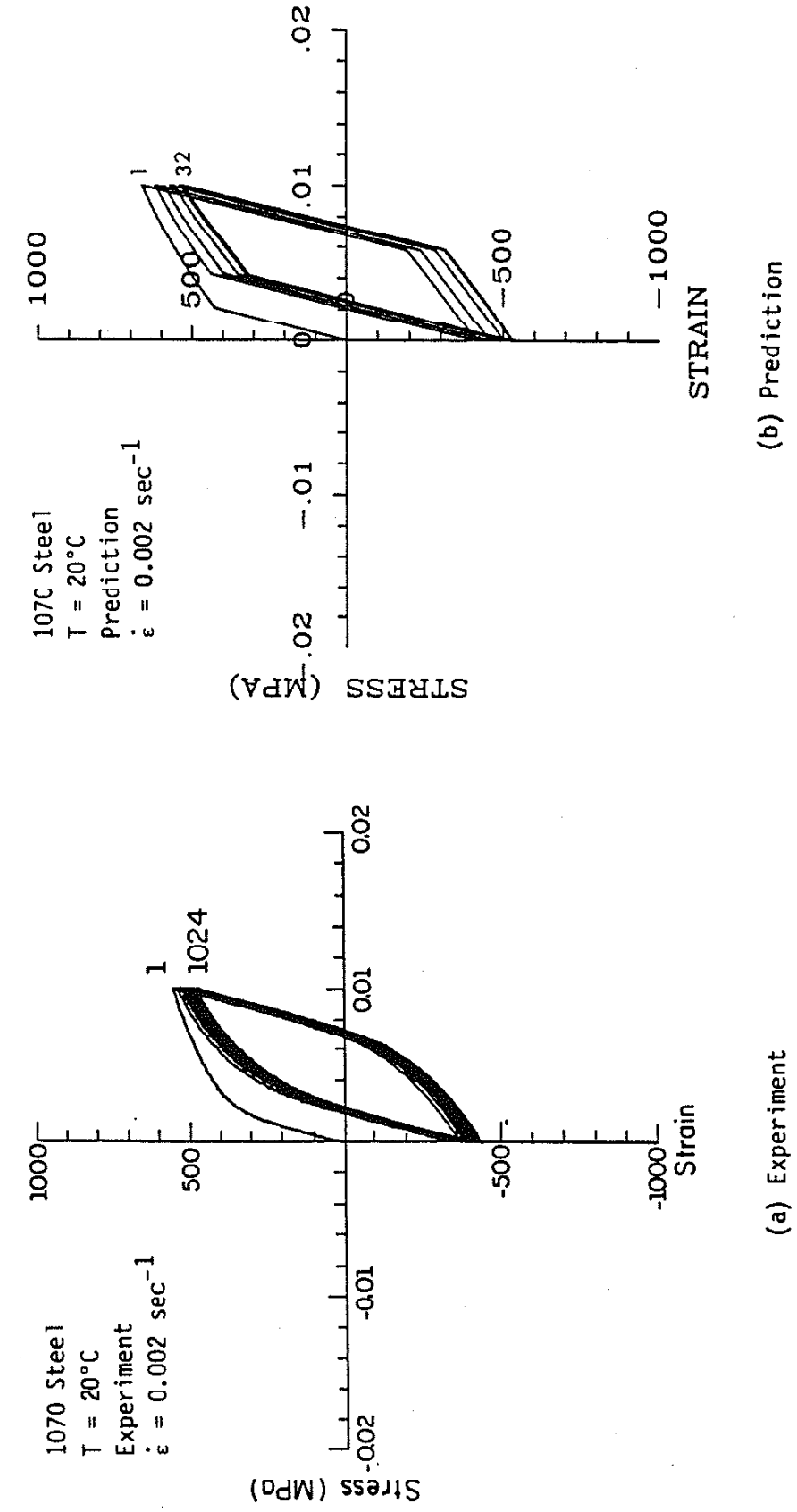

(a) Experiment (b) Prediction

Figure 29 Comparison of Isothermal Experimental and Predicted Mean Stress Relaxation, for T = 20°C, ε_{max} = 1.0%, ε_{min} = 0%, $\dot{\varepsilon}$ = 0.002 sec^{-1}

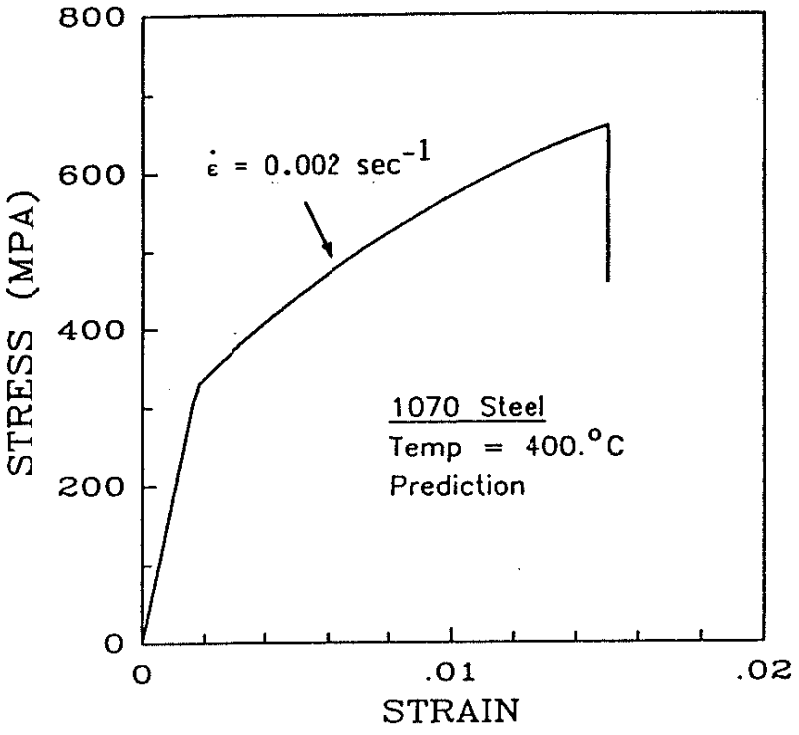

(a) Predicted Stress-Strain Response

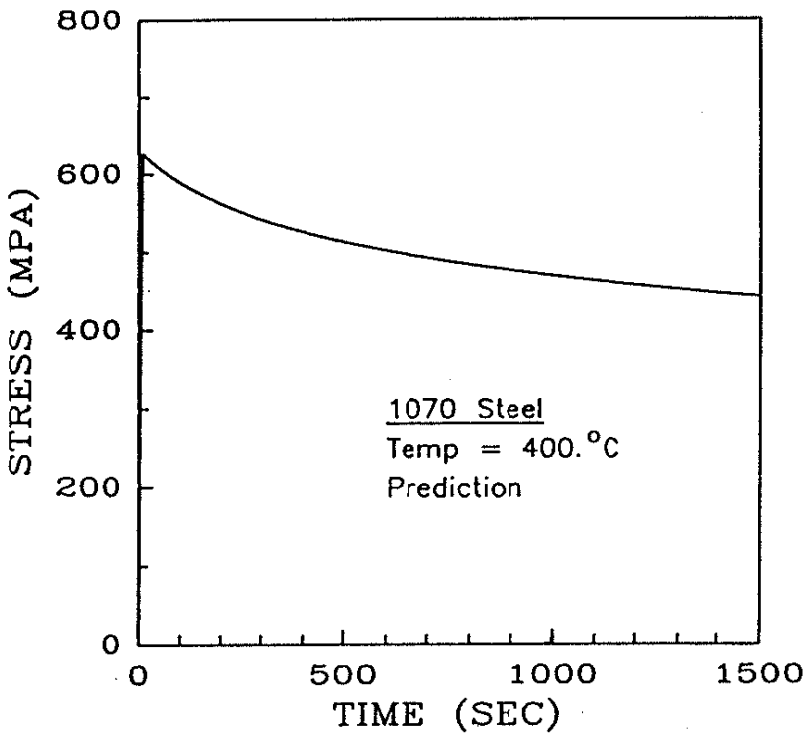

(b) Predicted Stress Relaxation-Time Response

Figure 30 Strain Hold Stress Relaxation Predictions at 400°C

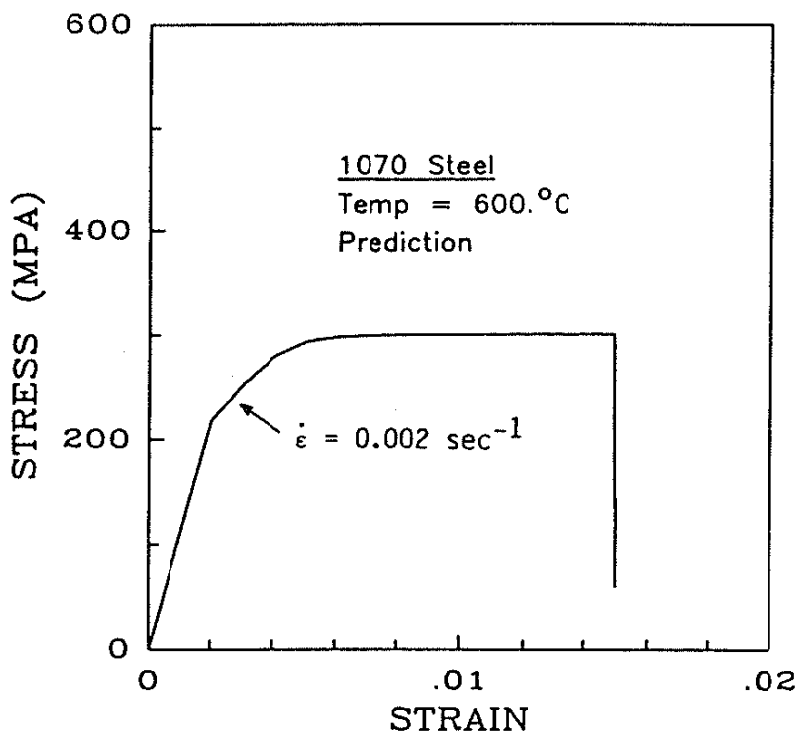

(a) Predicted Stress-Strain Response

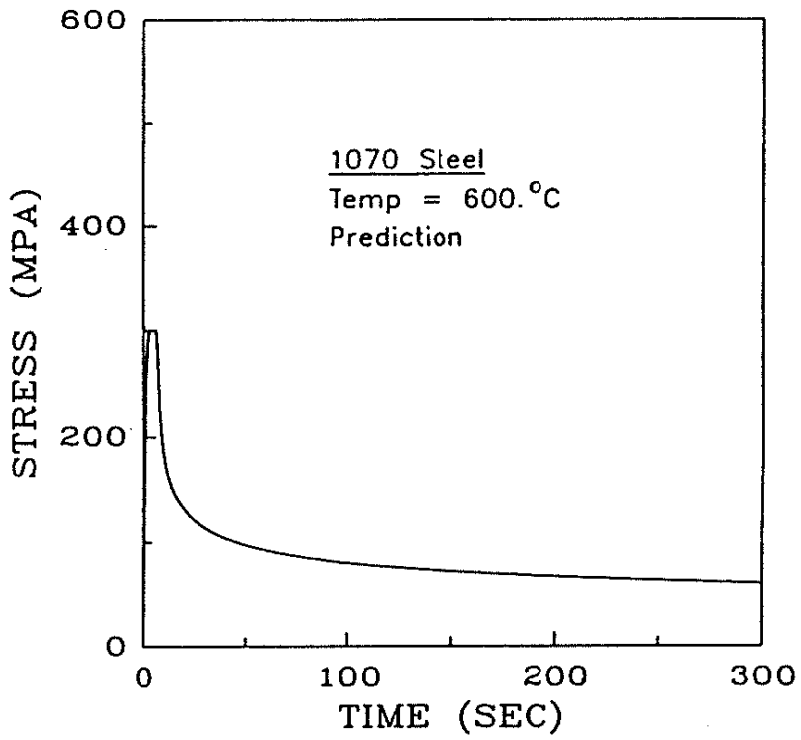

(b) Predicted Stress Relaxation-Time Response

Figure 31 Strain Hold Stress Relaxation Predictions at 600°C

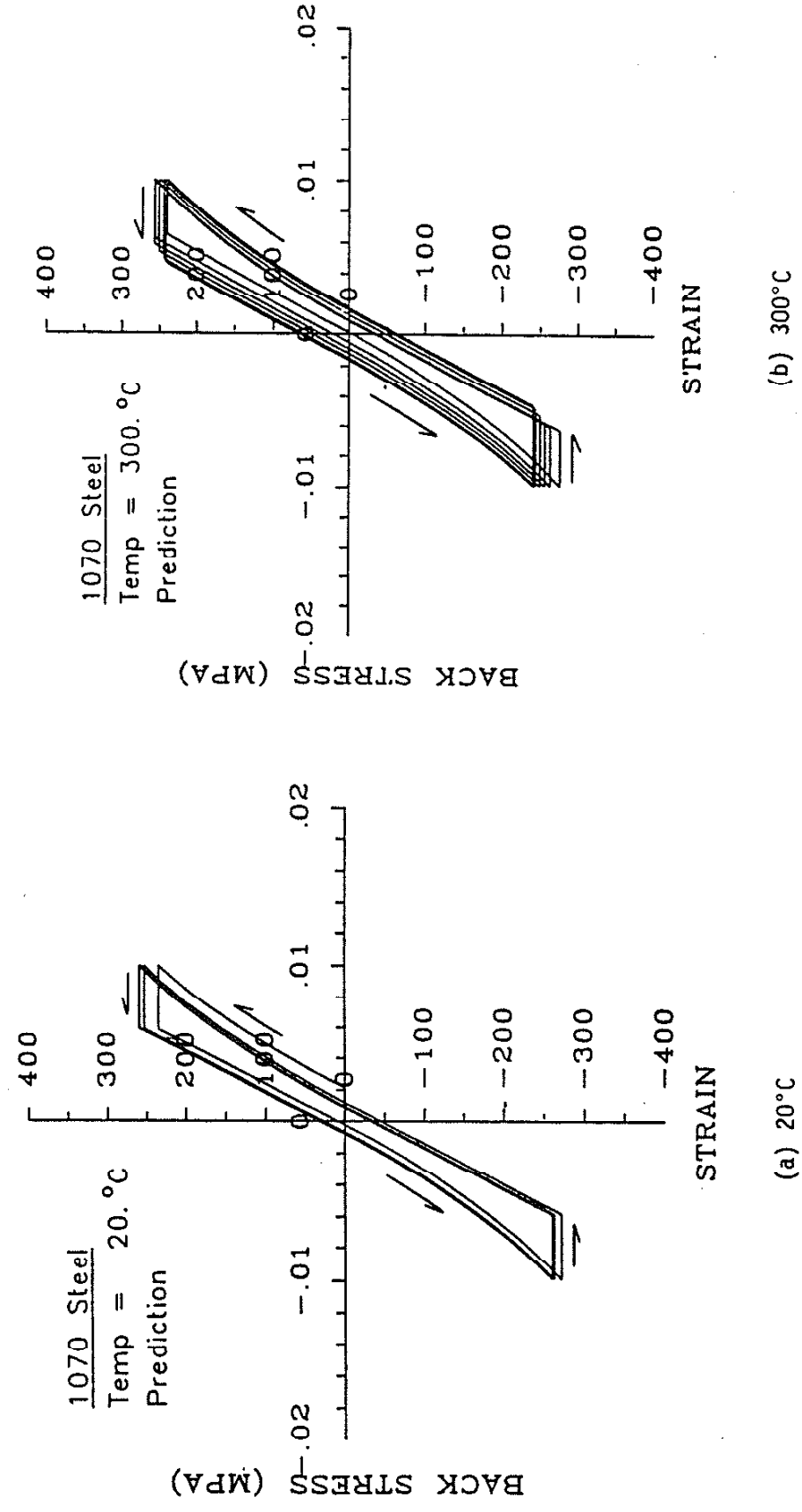

Figure 32 Predicted Back Stress Strain Response for $\dot{\varepsilon} = 0.002\ sec^{-1}$

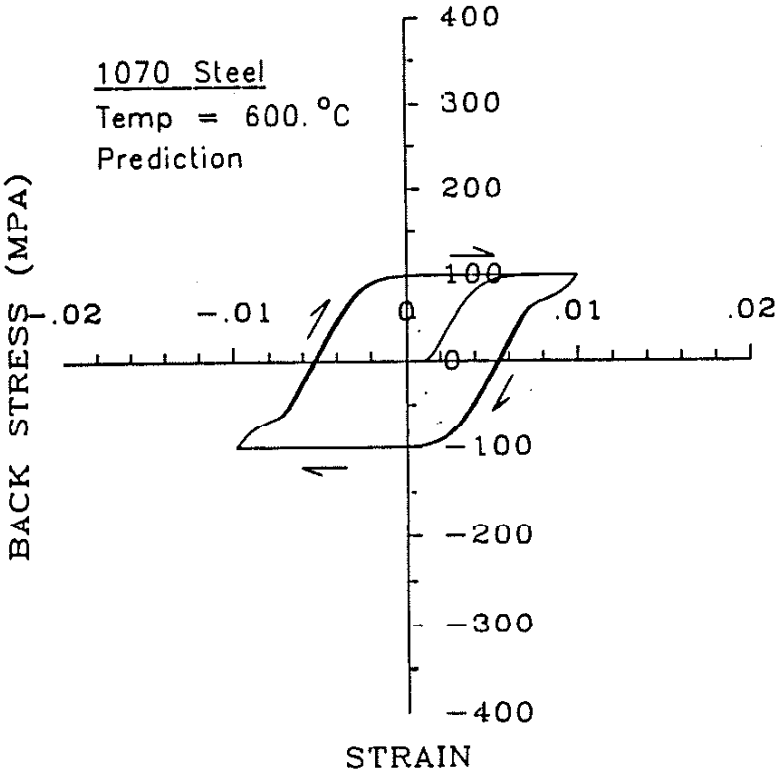

(c) 600°C

Figure 32 (continued)

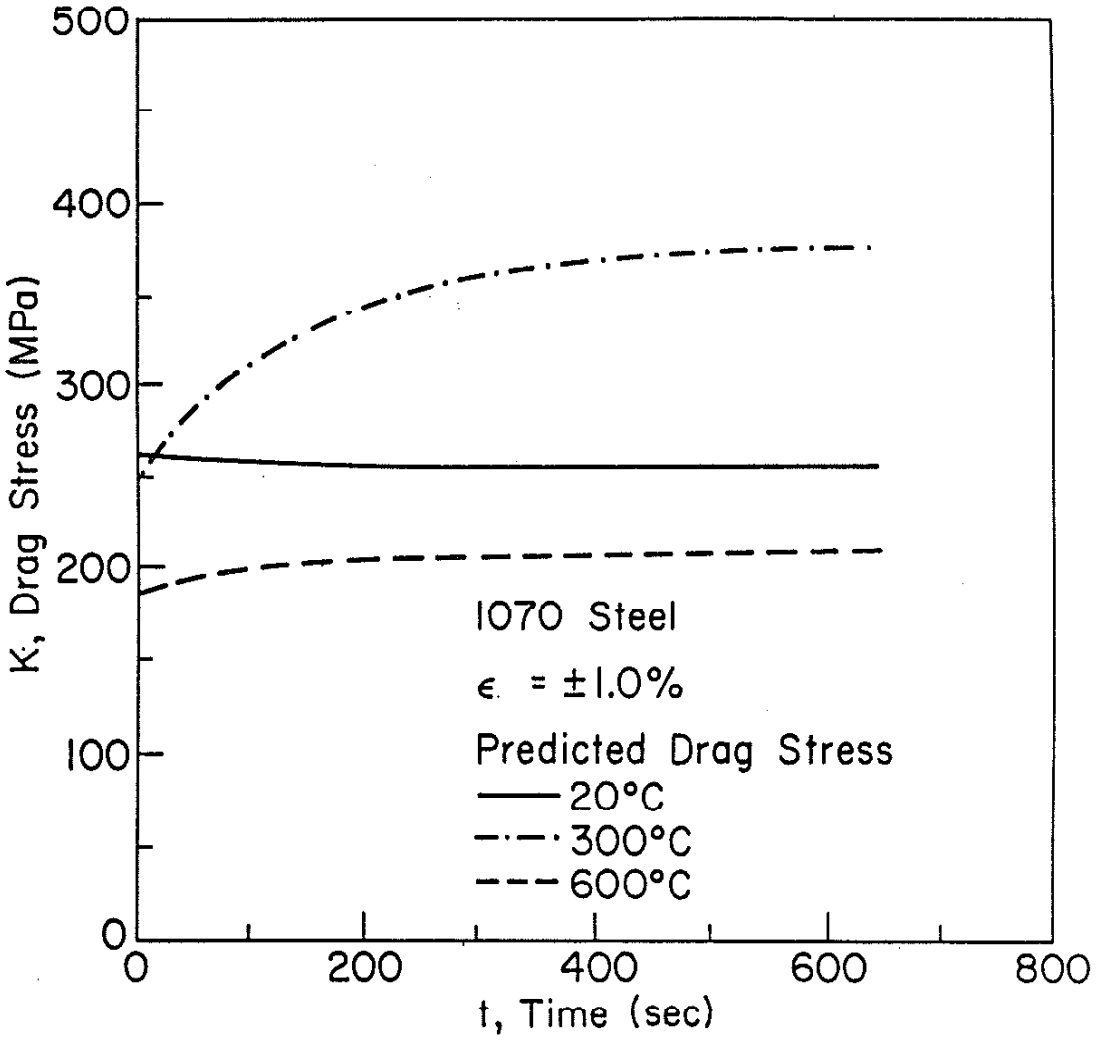

Figure 33 Predicted Drag Stress Evolution
for ϵ_a = ±1.0%, and $\dot{\epsilon}$ = 0.002 sec^{-1}

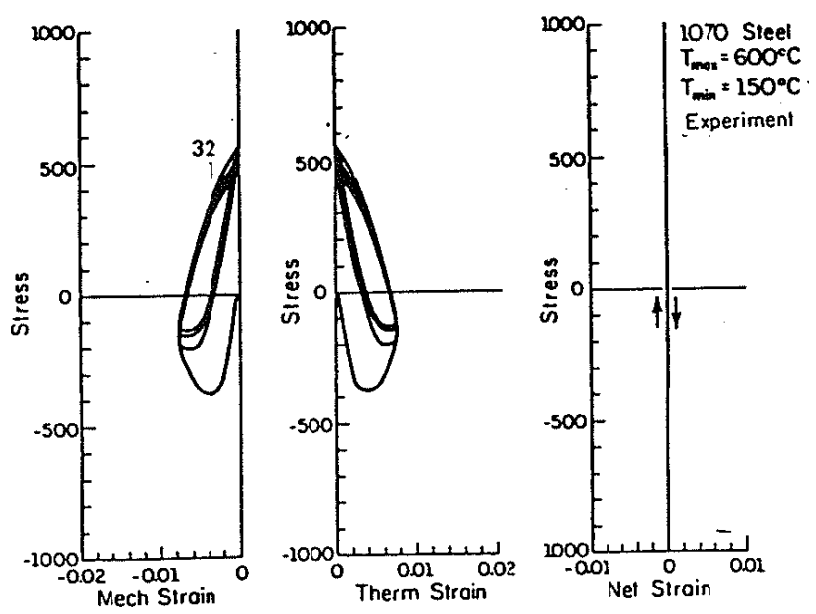

(a) Experiment

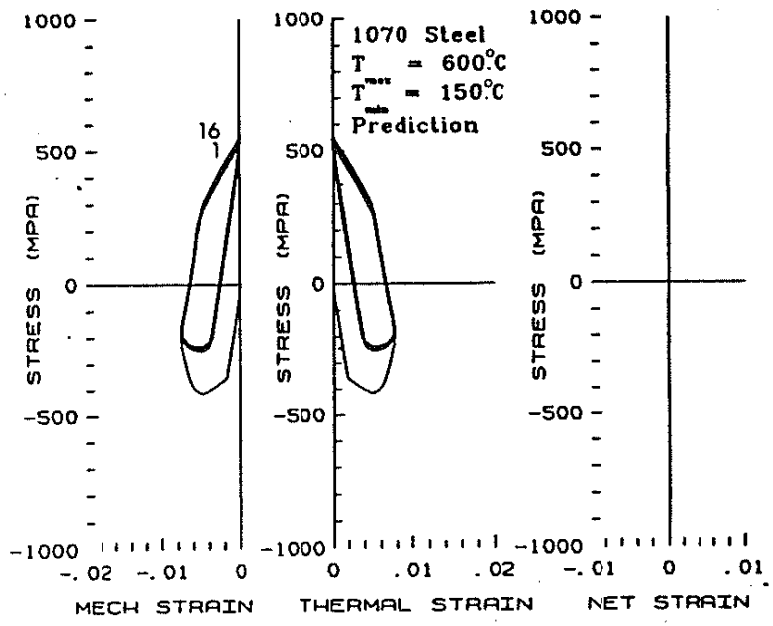

(b) Prediction

Figure 34 Comparison of Total Constraint Thermo-Mechanical Experimental and Predicted Material Response for T_{max} = 600°C, T_{min} = 150°C

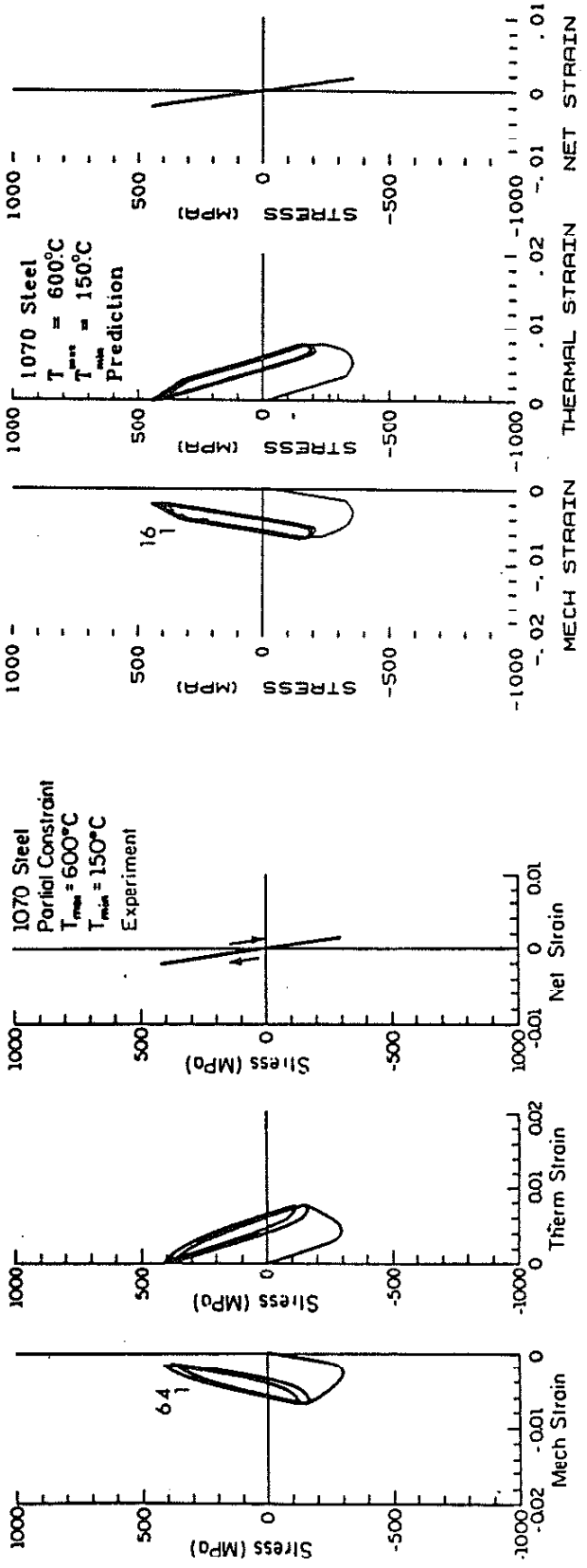

(a) Experiment (b) Prediction

Figure 35 Comparison of Partial Constraint Thermo-Mechanical Experimental and Predicted Material Response for T_{max} = 600°C, T_{min} = 150°C

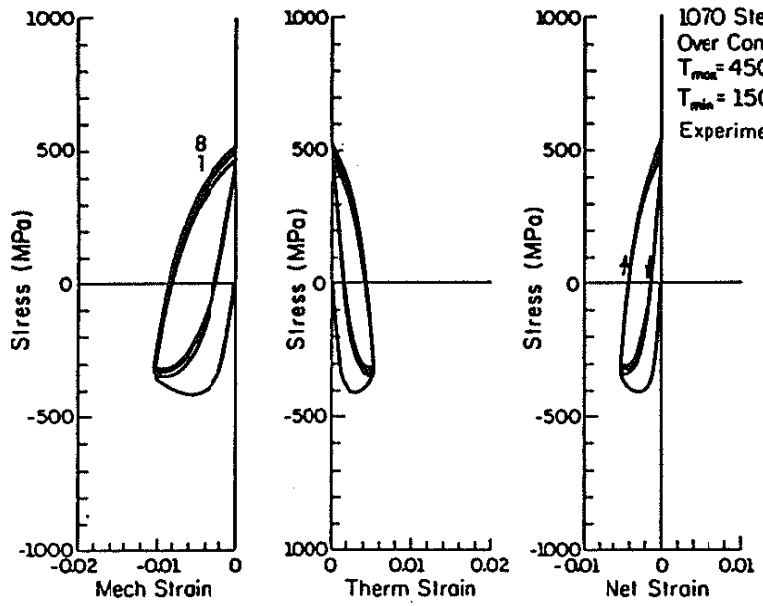

(a) Experiment

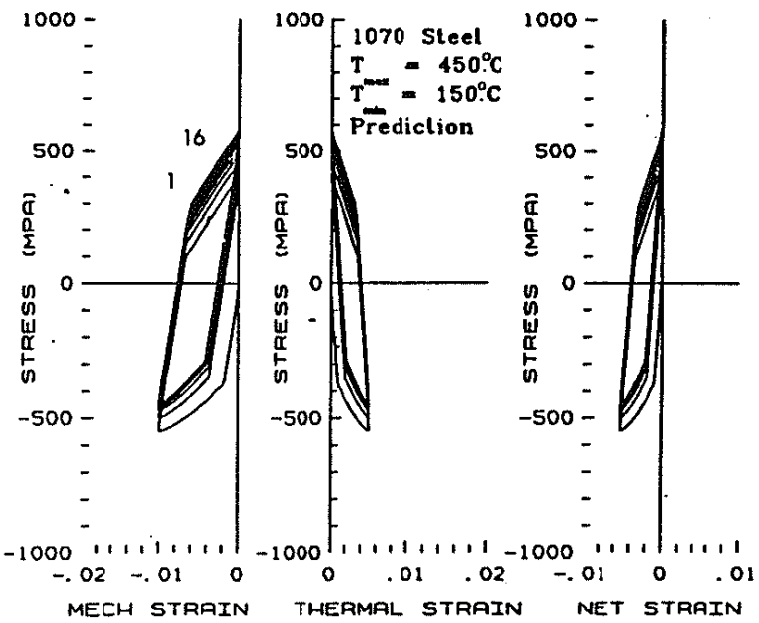

(b) Prediction

Figure 36 Comparison of Over Constraint Thermo-Mechanical Experimental and Predicted Material Response for T_{max} = 450°C, T_{min} = 150°C

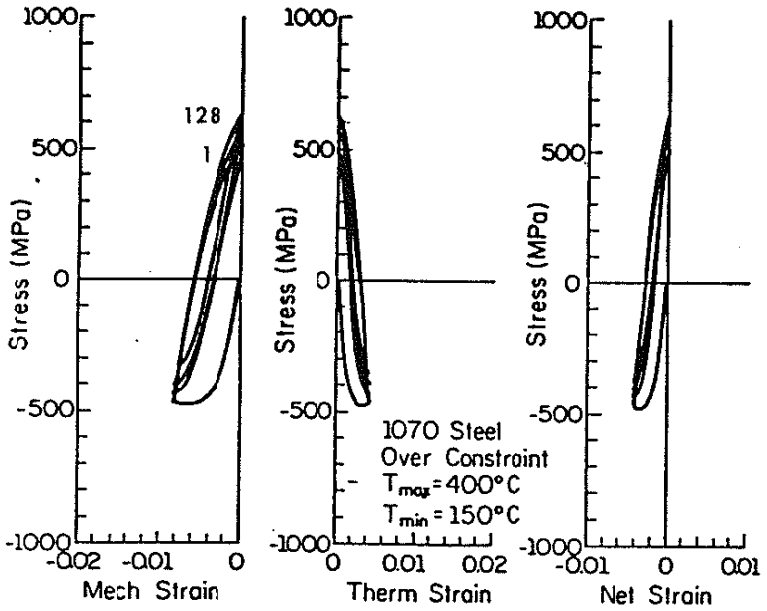

(a) Experiment

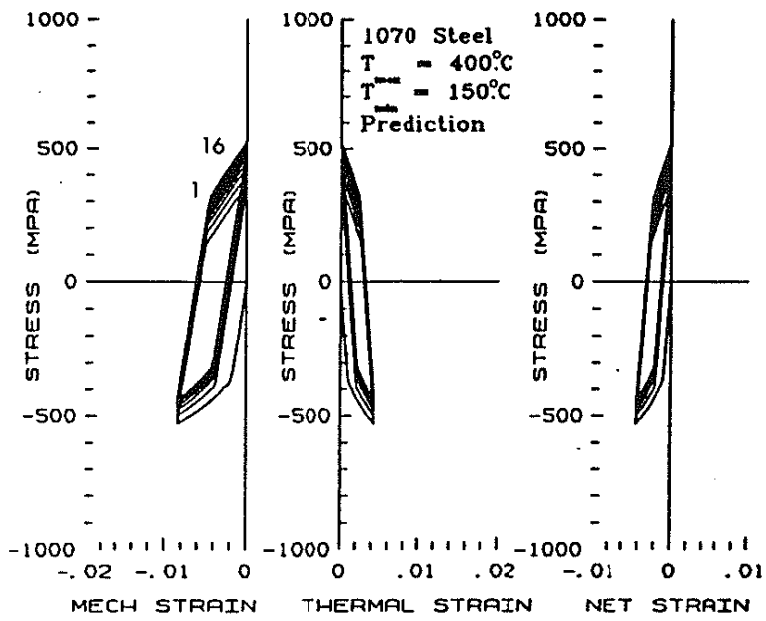

(b) Prediction

Figure 37 Comparison of Over Constraint Thermo-Mechanical Experimental and Predicted Material Response for T_{max} = 400°C, T_{min} = 150°C

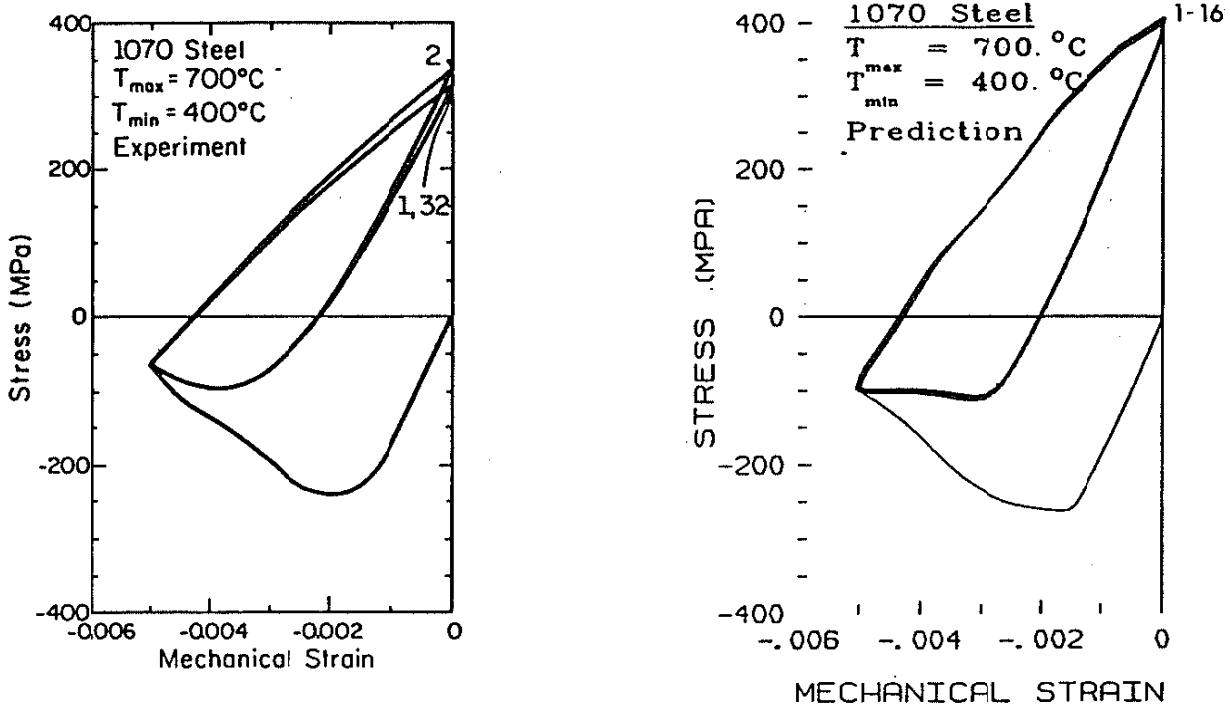

(a) Experiment

(b) Prediction

Figure 38 Comparison of Total Constraint Thermo-Mechanical Experimental and Predicted Material Response for T_{max} = 700°C, T_{min} = 400°C

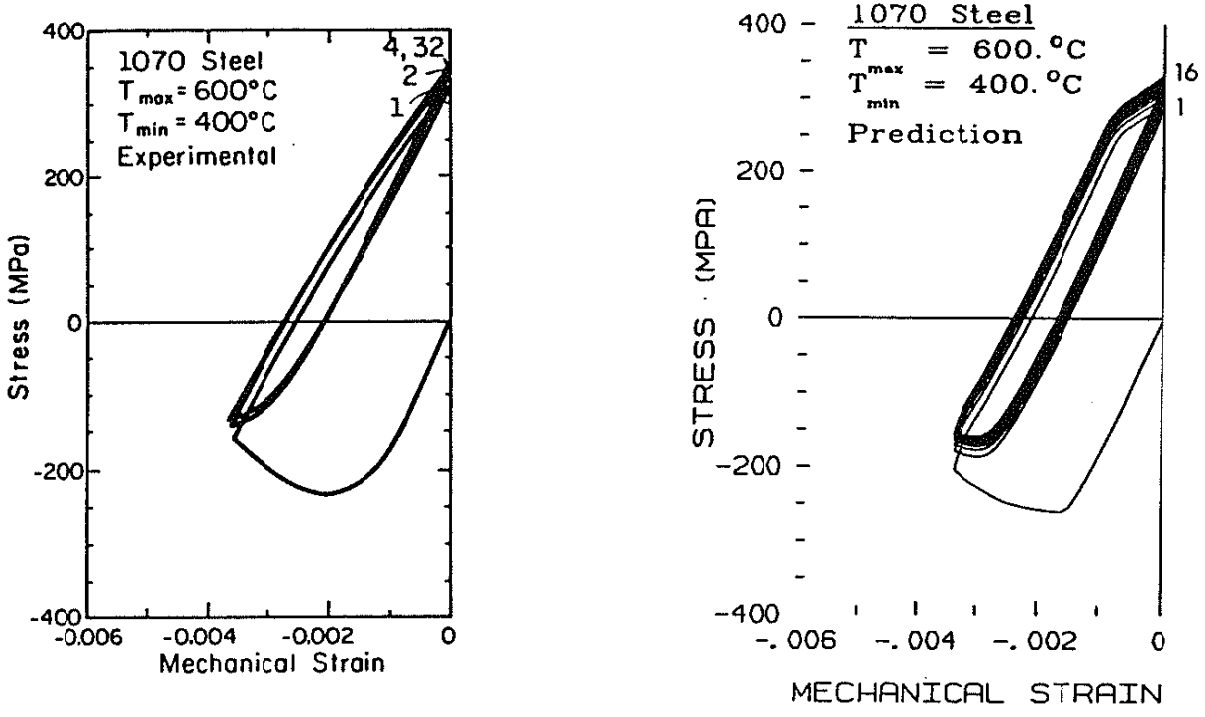

(a) Experiment

(b) Prediction

Figure 39 Comparison of Total Constraint Thermo-Mechanical Experimental and Predicted Material Response for T_{max} = 600°C, T_{min} = 400°C

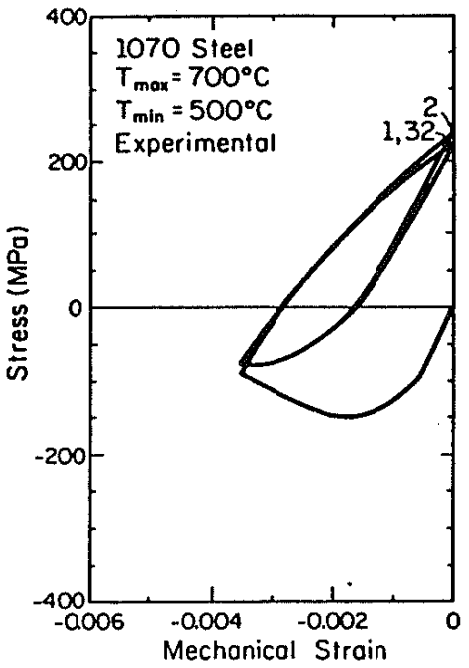

(a) Experiment

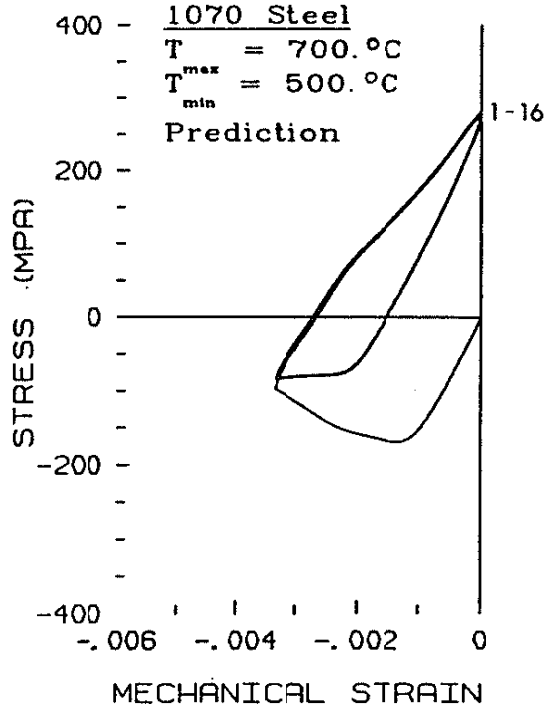

(b) Prediction

Figure 40 Comparison of Total Constraint Thermo-Mechanical Experimental and Predicted Material Response for T_{max} = 700°C, T_{min} = 500°C

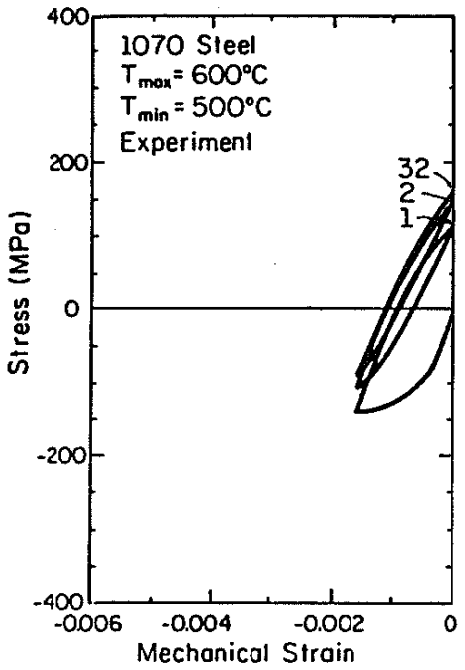

(a) Experiment

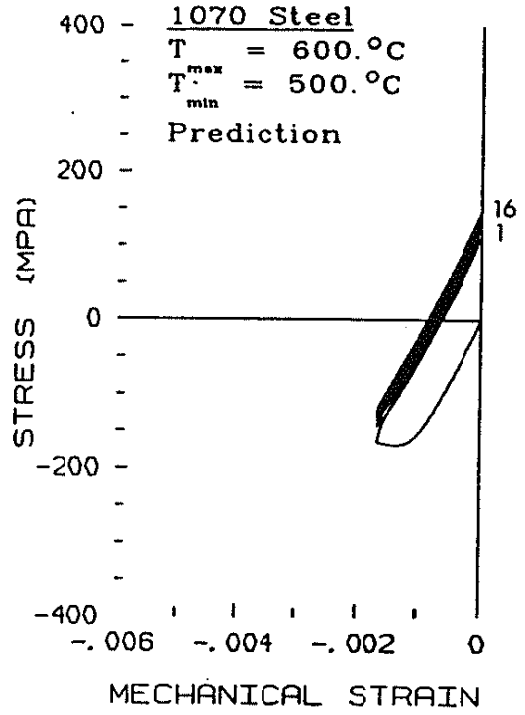

(b) Prediction

Figure 41 Comparison of Total Constraint Thermo-Mechanical Experimental and Predicted Material Response for T_{max} = 600°C, T_{min} = 500°C

8. REFERENCES

1. Pugh, C. E., and Robinson, D. N., "Some Trends in Constitutive Equation Model Development for High-Temperature Behavior of Fast-Reactor Structural Alloys," Nuclear Engineering and Design, Vol. 47, pp. 269-276, 1978.

2. Martin, J. F., "Fatigue Damage Analysis for Irregular Shaped Structures Subjected to Representative Loads," Ph.D. Thesis, Dept. of Mechanical and Industrial Engineering at the University of Illinois at Urbana-Champaign, 1973.

3. Walker, K. P., "Research and Development Program for Non-Linear Structural Modelling with Advanced Time-Temperature Dependent Constitutive Relationships," PWA-5700-SO, United Technologies Research Center, (also NASA CR-165533), 1981.

4. Nonlinear Constitutive Relations for High Temperature Applications - 1984, NASA Conference Publication 2369, June 1984.

5. Drucker, D. C., and Palgen, L., "On Stress-Strain Relations Suitable for Cyclic and Other Loading," J. Applied Mechanics, Vol. 48, pp. 479-485, 1981.

6. Cook, T. S., Kim, K. S., and McKnight, R. L., "Thermal Mechanical Fatigue of Cast Rene '80," ASTM Symposium on Low Cycle Fatigue, New York, October 1985.

7. Krieg, R. D., "A Practical Two Surface Plasticity Theory," J. of Applied Mechanics, pp. 641-646, September 1975.

8. Lambda, H. S., "Nonproportional Cyclic Plasticity," TAM report No. 413, Dept. of Theoretical and Applied Mechanics, University of Illinois at Urbana-Champaign, 1976.

9. Garud, Y. S., "A New Approach to the Evaluation of Fatigue Under Multi-axial Loadings," J. of Engineering Materials and Technology, Vol. 103, 1981.

10. McDowell, D. L., "A Two-Surface Model for Transient Nonproportional Cyclic Plasticity: Part I - Development of Appropriate Equations, and : Part II - Comparison of Theory with Experiments," ASME Journal of Applied Mechanics, Vol. 52, pp. 298-308, June 1985.

11. Bodner, S. R., and Partom, Y., "Constitutive Equations for Elastic-Viscoplastic Strain Hardening Materials," J. of Applied Mechanics, Vol. 42, pp. 385-389, 1975.

12. Bodner, S. R., and Partom, I., and Partom, Y., "Uniaxial Cyclic Loading of Elastic-Viscoplastic Materials," J. of Applied Mechanics, Vol. 46, 1975, pp. 805-810.

13. Bodner, S. R., and Merzer, A., "Viscoplastic Constitutive Equations for Copper with Strain Rate History and Temperature Effects," J. of Engineering Materials and Technology, Vol. 100, pp. 388-394, 1978.

14. Miller, A., "An Inelastic Constitutive Model for Monotonic, Cyclic, and Creep Deformation: Part I and Part II," J. of Engineering Materials and Technology, Vol. 98, pp. 97-113, April 1976.

15. Hart, E. W., "Constitutive Relations for the Nonelastic Deformation of Metals," J. of Engineering Materials and Technology, Vol. 98, 1976, pp. 193-202.

16. Onat, E. T., "Representation of Inelastic Behavior," Yale University Subcontract Report to Oak Ridge National Laboratory, ORNL/Sub/3863-2, November 1976.

17. Porter, A. R. S., and Leckie, F. A., "Constitutive Relationships for the Time-Dependent Deformation of Metals," J. of Engineering Materials and Technology, Vol. 98, January 1976.

18. Robinson, D. N., and Swindeman, R. W., "Unified Creep-Plasticity Constitutive Equations for 2-1/4 Cr-1 Mo Steel at Elevated Temperatures," ORNL/TM-8444, October 1982.

19. Cescotto, S., Leckie, F., and Abrahamson, E., "Unified Constitutive Models for Creep and Plasticity at High Temperatures," University of Illinois at Urbana-Champaign, 1982.

20. Abrahamson, T. E., "Modeling the Behavior of Type 304 Stainless Steel with a Unified Creep-Plasticity Theory," Ph.D. Thesis, Dept. of Mechanical and Industrial Engineering at the University of Illinois at Urbana-Champaign, 1983.

21. Slavik, D. C., and Sehitoglu, H., "Constitutive Models Suitable for Thermal Loading," to appear in J. of Engineering Materials and Technology, 1986.

22. Bailey, R. W., "Note on the Softening of Strain Hardening Metals and It's Relation to Creep," J. of Institute of Metals, Vol. 35, pp. 27-40, 1926.

23. Orowan, E. J., "The Creep of Metals," West Scotland Iron and Steel Institute, Vol. 54, pp. 45-53, 1946.

24. Frost, H. J., and Ashby, M. F., Deformation-Mechanism Maps, The Plasticity and Creep of Metals and Ceramics, Pergamon Press, 1982.

25. Sehitoglu, H., and Morrow, J., "Characterization of Thermo-Mechanical Fatigue," ASME PVP-71, Thermal and Environmental Effects in Fatigue: Research Design Interface, pp. 93-110, 1983.

26. Sehitoglu, H., "Constraint Effect in Thermo-Mechanical Fatigue," J. Engineering Materials and Technology, Vol. 107, pp. 221-226, July 1985.

27. Karasek, M., "An Investigation into Isothermal and Thermo-mechanical Fatigue Damage at Elevated Temperatures," M.S. Thesis, Dept. of Mechanical and Industrial Engineering at the University of Illinois at Urbana-Champaign, 1984.

28. Slavik, D. C., and Sehitoglu, H., "A Unified Creep-Plasticity Model Suitable for Thermo-Mechanical Loading," 3rd Symposium on Nonlinear Constitutive Relations for High Temperature Applications, Akron, Ohio, June 1986.

29. Tuegel, E. J., "An Investigation of a State Variable Representation of Plasticity," M.S. Thesis, Dept. of Mechanical and Industrial Engineering at the University of Illinois at Urbana-Champaign, 1981.